Министерство образования и науки Российской Федерации
федеральное государственное автономное образовательное учреждение
высшего образования
**«НАЦИОНАЛЬНЫЙ ИССЛЕДОВАТЕЛЬСКИЙ
ТОМСКИЙ ПОЛИТЕХНИЧЕСКИЙ УНИВЕРСИТЕТ»**

Институт Физико-технический
Направление подготовки 03.04.02 Физика конденсированного состояние вещества
Кафедра Общей физики

МАГИСТЕРСКАЯ ДИССЕРТАЦИЯ

Тема работы
Разработка и анализ двумерных решеточных структур для получения рентгеновских изображений из одного снимка

УДК 681.785.552:621.386

Студент

Группа	ФИО	Подпись	Дата
0БМ51	Захарова Маргарита Анатольевна		

Руководитель

Должность	ФИО	Ученая степень, звание	Подпись	Дата
Профессор	Крючков Юрий Юрьевич	д.ф.-м. н.		

КОНСУЛЬТАНТЫ:

По разделу «Финансовый менеджмент, ресурсоэффективность и ресурсосбережение»

Должность	ФИО	Ученая степень, звание	Подпись	Дата
Доцент	Рыжакина Татьяна Гавриловна			

По разделу «Социальная ответственность»

Должность	ФИО	Ученая степень, звание	Подпись	Дата
Профессор	Федорчук Юрий Митрофанович	д.т.н.		

Консультант – лингвист кафедры Общей физики

Должность	ФИО	Ученая степень, звание	Подпись	Дата
Доцент	Емельянов Игорь Леонидович	к.социол.н.		

ДОПУСТИТЬ К ЗАЩИТЕ:

Зав. кафедрой	ФИО	Ученая степень, звание	Подпись	Дата
Общей физики	Лидер Андрей Маркович	к.ф.-м.н.		

Томск – 2017 г

Запланированные результаты обучения

по основной образовательной программе высшего профессионального образования, направление подготовки 03.04.02 Физика, профиль Физика конденсированного состояния вещества

Код результата	Результат обучения (Выпускник должен быть готов)
Общекультурные (универсальные) компетенции	
Р1	Понимает необходимость самостоятельного обучения и повышения квалификации в течение всего периода профессиональной деятельности.
Р2	Проявляет способность эффективно работать самостоятельно в качестве члена команды по междисциплинарной тематике, быть лидером в команде, консультировать по вопросам проектирования научных исследований, а также быть готовым к педагогической деятельности.
Р3	Умеет находить зарубежных и отечественных партнеров, владеет иностранным языком, позволяющим работать с зарубежными партнерами с учетом культурных, языковых и социально-экономических условий.
Р4	Проявляет понимание используемых методов, области их применения, вопросов безопасности и здравоохранения, юридических аспектов, ответственности за профессиональную деятельность и ее влияния на окружающую среду.
Р5	Следует кодексу профессиональной этики, ответственности и нормам научно-исследовательской деятельности.
Профессиональные компетенции	
Р6	Проявляет глубокие естественнонаучные, математические профессиональные знания в проведении научных исследований в перспективных областях профессиональной деятельности.
Р7	Принимает участие в фундаментальных исследованиях и проектах в области физики металлов и материаловедения, а также в модернизации современных и создании новых методов изучения механических, электрических, магнитных, тепловых свойств твердых тел.
Р8	Способен обрабатывать, анализировать и обобщать научно-техническую информацию, передовой отечественный и зарубежный опыт в профессиональной деятельности, осуществлять презентацию научной деятельности.
Р9	Способен применять полученные знания для решения нечетко определенных задач, в нестандартных ситуациях, использует творческий подход для разработки новых оригинальных идей и методов исследования в области физики металлов, материаловедения и термообработки.
Р10	Способен планировать проведение аналитических имитационных исследований по профессиональной деятельности с применением современных достижений науки и техники, передового отечественного и зарубежного опыта в области научных исследований, умеет критически оценивать полученные теоретические и экспериментальные данные и делает выводы, знает правовые основы в области интеллектуальной собственности.
Р11	Умеет интегрировать знания в различных и смежных областях научных исследований и решает задачи, требующие абстрактного и креативного мышления и оригинальности в разработке концептуальных аспектов проектов научных исследований.

Министерство образования и науки Российской Федерации
федеральное государственное автономное образовательное учреждение
высшего образования
**«НАЦИОНАЛЬНЫЙ ИССЛЕДОВАТЕЛЬСКИЙ
ТОМСКИЙ ПОЛИТЕХНИЧЕСКИЙ УНИВЕРСИТЕТ»**

Институт физико-технический
Направление подготовки 03.04.02 Физика конденсированного состояние вещества
Кафедра общей физики

УТВЕРЖДАЮ:
Зав. кафедрой
_____ _____ _А.М.Лидер_
(Подпись) (Дата) (Ф.И.О.)

ЗАДАНИЕ
на выполнение выпускной квалификационной работы

В форме:

Магистерской диссертации

(бакалаврской работы, дипломного проекта/работы, магистерской диссертации)

Студенту:

Группа	ФИО
0БМ51	Захаровой Маргарите Анатольевне

Тема работы:

Разработка и анализ двумерных решеточных структур для получения рентгеновских изображений из одного снимка	
Утверждена приказом директора (дата, номер)	

Срок сдачи студентом выполненной работы:	

ТЕХНИЧЕСКОЕ ЗАДАНИЕ:

Исходные данные к работе *(наименование объекта исследования или проектирования; производительность или нагрузка; режим работы (непрерывный, периодический, циклический и т. д.); вид сырья или материал изделия; требования к продукту, изделию или процессу; особые требования к особенностям функционирования (эксплуатации) объекта или изделия в плане безопасности эксплуатации, влияния на окружающую среду, энергозатратам; экономический анализ и т. д.).*	– двумерные дифракционные решетки периодом 50 мкм; – двумерные дифракционные решетки периодом 25 мкм; – двумерные дифракционные решетки периодом 10 мкм. Материалы изделия: кремниевый диск, активатор адгезии, негативный фоторезист, проявитель, золото.
Перечень подлежащих исследованию, проектированию и разработке вопросов *(аналитический обзор по литературным источникам с целью выяснения достижений мировой науки техники в рассматриваемой области; постановка задачи исследования, проектирования, конструирования; содержание процедуры исследования, проектирования, конструирования; обсуждение результатов выполненной работы; наименование дополнительных разделов, подлежащих разработке; заключение по работе).*	– проведение литературного обзора; – постановка задачи исследования; – адаптация технологического процесса оптической литографии для изготовления двумерных дифракционных решеток; – изготовление двумерных решеток; – оптимизация технологического процесса на основе полученных данных; – исследование качества решеток с использованием растровой электронной микроскопии; – разработка алгоритма оценки эффективности решеток в

	радиографической установке; – тестирование и оценка качества решеток в радиографической установке; – обсуждение результатов; – заключение.
Перечень графического материала	**-**

Консультанты по разделам выпускной квалификационной работы

Раздел	Консультант
Социальная ответственность	Федорчук Юрий Митрофанович
Финансовый менеджмент, ресурсоэффективность и ресурсосбережение	Рыжакина Татьяна Гавриловна
Консультант-лингвист	Емельянов Игорь Леонидович

Названия разделов, которые должны быть написаны на русском и иностранном языках:

научная работа выполнена на английском языке

Дата выдачи задания на выполнение выпускной квалификационной работы по линейному графику	

Задание выдал руководитель:

Должность	ФИО	Ученая степень, звание	Подпись	Дата
Профессор	Крючков Юрий Юрьевич	д.ф.-м.н.		

Задание принял к исполнению студент:

Группа	ФИО	Подпись	Дата
0БМ51	Захарова Маргарита Анатольевна		

ЗАДАНИЕ ДЛЯ РАЗДЕЛА
«ФИНАНСОВЫЙ МЕНЕДЖМЕНТ, РЕСУРСОЭФФЕКТИВНОСТЬ И РЕСУРСОСБЕРЕЖЕНИЕ»

Студенту:

Группа	ФИО
0БМ51	Захаровой Маргарита Анатольевне

Институт	ФТИ	Кафедра	ОФ
Уровень образования	Магистратура	**Направление/ специальность**	03.04.02 Физика конденсированного состояния вещества

Исходные данные к разделу «Финансовый менеджмент, ресурсоэффективность и ресурсосбережение»:	
1. *Стоимость ресурсов научного исследования (НИ): материально-технических, энергетических, финансовых, информационных и человеческих*	Использование информации, представленной в российских и иностранных научных публикациях, аналитических материалах и изданиях, нормативно-правовых документах.
2. *Нормы и нормативы расходования ресурсов*	
3. *Используемая система налогообложения, ставки налогов, отчислений, дисконтирования и кредитования*	
Перечень вопросов, подлежащих исследованию, проектированию и разработке:	
1. *Оценка коммерческого потенциала, перспективности и альтернатив проведения НИ с позиции ресурсоэффективности и ресурсосбережения*	Проведение предпроектного анализа. Определение целевого рынка и проведение его сегментирования. Выполнение SWOT-анализа проекта.
2. *Определение возможных альтернатив проведения научных исследований*	Определение целей и ожиданий, требований проекта. Определение заинтересованных сторон и их ожиданий.
3. *Планирование процесса управления НТИ: структура и график проведения, бюджет, риски.*	Составление календарного плана проекта. Определение бюджета НТИ
4. *Определение ресурсной, финансовой, экономической эффективностей.*	Проведение оценки экономической эффективности исследования.
Перечень графического материала *(с точным указанием обязательных чертежей):*	
1. *Оценка конкурентоспособности технических решений* 2. *Матрица SWOT* 3. *Оценка готовности проекта к коммерциализации* 4. *Календарный план-график и бюджет НТИ* 5. *Оценка ресурсной, финансовой и экономической эффективности НТИ* 6. *Сравнительная эффективность разработки*	

Дата выдачи задания для раздела по линейному графику	

Задание выдал консультант:

Должность	ФИО	Ученая степень, звание	Подпись	Дата
Доцент	Рыжакина Татьяна Гавриловна	к.э.н		

Задание принял к исполнению студент:

Группа	ФИО	Подпись	Дата
0БМ51	Захарова Маргарита Анатольевна		

ЗАДАНИЕ ДЛЯ РАЗДЕЛА
«СОЦИАЛЬНАЯ ОТВЕТСТВЕННОСТЬ»

Студенту:

Группа	**ФИО**
0БМ51	Захарова Маргарита Анатольевна

Институт	ФТИ	**Кафедра**	Общая физика
Уровень образования	Магистратура	**Направление/ специальность**	03.04.02 Физика конденсированного состояние вещества

ЗАДАНИЕ

Исходные данные к разделу «Социальная ответственность»:	
1. Описание рабочего места (рабочей зоны, технологического процесса, механического оборудования) на предмет возникновения: – *вредных проявлений факторов производственной среды (метеоусловия, вредные вещества, освещение, шумы, вибрации, электромагнитные поля, ионизирующие излучения)* – *опасных проявлений факторов производственной среды (механической природы, термического характера, электрической, пожарной и взрывной природы)* – *негативного воздействия на окружающую природную среду (атмосферу, гидросферу, литосферу)* – *чрезвычайных ситуаций (техногенного, стихийного, экологического и социального характера)*	1. Объектом исследования является матриксы из поли-L-молочной кислоты. К вредным факторам данной дипломной работы можно отнести микроклимат рабочего помещения, освещение рабочей зоны, электромагнитное поле и шум. К опасным факторам дипломной работы можно отнести возможность поражения электрическим током. Возможные чрезвычайные ситуации на рабочем месте: чрезвычайные ситуации техногенного характера (пожар) и чрезвычайные ситуации природного характера (резкое падение температуры воздуха окружающей среды).
2. Знакомство и отбор законодательных и нормативных документов по теме	2. Согласно всем видам вредных и опасных факторов дипломной работы отобраны и проанализированы соответствующие законодательные и нормативные документы.
Перечень вопросов, подлежащих исследованию, проектированию и разработке	
1. Анализ выявленных вредных факторов проектируемой производственной среды в следующей последовательности: – *физико-химическая природа вредности;* – *действие фактора на организм человека;* – *приведение допустимых норм с необходимой размерностью;* – *предлагаемые средства защиты.*	
2. Анализ выявленных опасных факторов проектируемой произведённой среды в следующей последовательности: *электробезопасность;*	
3. Охрана окружающей среды: *разработка решения по обеспечению экологической безопасности со ссылками на НТД по охране окружающей среды.*	

4. Защита в чрезвычайных ситуациях: *– перечень возможных ЧС на объекте (сильные морозы, диверсия);* *– выбор наиболее типичной ЧС;* *– разработка превентивных мер по предупреждению ЧС;* *– разработка мер по повышению устойчивости объекта к данной ЧС;* *разработка действий в результате возникшей ЧС и мер по ликвидации её последствий;*
5. Правовые и организационные вопросы обеспечения безопасности: *– специальные (характерные для проектируемой рабочей зоны) правовые нормы трудового законодательства;*
6. Схемы: *– план эвакуации;* *– план размещения светильников на потолке.*

Дата выдачи задания для раздела по линейному графику	

Задание выдал консультант:

Должность	**ФИО**	**Ученая степень, звание**	**Подпись**	**Дата**
Профессор	Федорчук Юрий Митрофанович	д.т.н.		

Министерство образования и науки Российской Федерации
Федеральное государственное автономное образовательное учреждение
высшего профессионального образования
**«НАЦИОНАЛЬНЫЙ ИССЛЕДОВАТЕЛЬСКИЙ
ТОМСКИЙ ПОЛИТЕХНИЧЕСКИЙ УНИВЕРСИТЕТ»**

Физико-технический институт
Направление подготовки – физика
Кафедра общей физики
Уровень образования – магистр
Период выполнения – весенний семестр 2016/2017 учебного года

Форма представления работы:

магистерская диссертация

КАЛЕНДАРНЫЙ РЕЙТИНГ-ПЛАН
выполнения выпускной квалификационной работы

Срок сдачи студентом выполненной работы:	

Дата контроля	Название раздела (модуля) / вид работы (исследования)	Максимальный балл раздела (модуля)
15.03.2017 г.	Обзор литературы	20
20.04.2017 г.	Объект и методы исследования	20
25.05.2017 г.	Расчет и аналитика	20
23.05.2017 г.	Финансовый менеджмент, ресурсоэффективность и ресурсосбережение	15
29.05.2017 г.	Социальная ответственность	10
27.05.2017 г.	Обязательное приложение на иностранном языке*	15

*научная работа выполнена на английском языке

Составил преподаватель:

Должность	ФИО	Учёная степень, звание	Подпись	Дата
Ассистент КОФ	Лаптев Р.С.	к.т.н.		

СОГЛАСОВАНО:

Зав. Кафедрой	ФИО	Учёная степень, звание	Подпись	Дата
Общей физики	Лидер А.М.	к.ф.-м.н.		

Summary

The master thesis contains 102 pages, 41 figure, 35 tables and 38 literary sources.

Keywords: X-ray imaging, Single-shot imaging, X-ray gratings, UV LIGA, micropatterning.

The object of research: two-dimensional X-ray absorption gratings.

The objective: to develop high-quality two-dimensional X-ray gratings to be used in the single-shot imaging setups. Ultraviolet lithography and electroforming were used to manufacture the gratings; scanning electron microscopy and X-ray radiography were applied for grating quality characterization.

Recently developed grating-based single-shot X-ray imaging techniques have attracted a lot of interest due to unique information they provide on the inner structure of the objects within robust radiographic setup. The quality of the images for these techniques depends on the optical component in use, thus intended high-quality X-ray gratings are required.

In the course of the research: the method of optical lithography and electroforming was adapted to fabricate two-dimensional gratings, the photoresist characteristics necessary for the technological process were studied, the gratings were manufactured and their quality was examined by optical and scanning electron microscopy, and also using the developed algorithm for estimating the efficiency of gratings performance in radiographic setup.

As a **result of the research**, high-quality two-dimensional X-ray gratings were developed, as well as an algorithm for evaluating their quality and efficiency.

The gratings developed have a size of 1 cm x 1 cm, periods of 50, 25, 10 μm and thicknesses from 7 to 32 μm. These gratings are ready for use in installations with X-ray energies up to 28 keV.

Degree of implementation: the data are tested at international conferences in Finland and Brazil, as well as reported in seminars at Institute of Microstructure Technology of Karlsruhe Institute of Technology. The manuscript based on acquired results is in preparation.

Application: medical imaging, materials characterization.

Outlook: In the future, it is planned to continue the work towards improving the characteristics of gratings by using other photoresist compositions and X-ray lithography to obtain structures with a high aspect ratio that can be used at higher X-ray energies. It is planned to use the developed gratings in X-ray imaging setups to address scientific issues in the field of medicine and materials science. With the help of the developed gratings, a

significant improvement in the quality of the images is expected. In addition, it is planned to study the possibilities of using a spatial harmonic single-shot imaging with the sensitivity of the small-angle scattering signal to particle size.

The following theses and results are subjected to defense:

1) the technological process of fabrication of two-dimensional X-ray gratings based on ultraviolet lithography and gold electroforming, ensuring a high degree of periodicity of structures;

2) algorithm for estimation of the two-dimensional gratings quality and the efficiency of the wavefront modulation caused by the grating.

Реферат

Магистерская диссертация содержит 102 страницы, 41 цифру, 35 таблиц и 38 литературных источников.

Ключевые слова: рентгеновское изображение из одного снимка, рентгеновские решетки, ультрафиолетовая литография, гальванопластика, микроструктурирование.

Объект исследования: двумерные рентгеновские абсорбционные решетки. **Цель магистерской диссертации:** разработать высококачественные двухмерные рентгеновские решетки для использования в радиографических установках с целью получения изображений из одного снимка. Для изготовления решеток была использована ультрафиолетовая литография и гальванопластика; растровая электронная микроскопия и рентгеновская радиография были применены для оценки качества и эффективности работы решетки.

Недавно разработанные технологии рентгеновской визуализации на основе дифракционных решетчатых структур вызвали большой интерес благодаря уникальной информации о внутренней структуре объектов, которая может быть получена в радиографической установке. Качество изображений, получаемых с помощью этого метода, определяется качеством используемого оптического компонента. Таким образом, использование высококачественных рентгеновских решеток может существенно улучшить качество получаемой информации.

В процессе исследования проводились работы по адаптации метода оптической литографии и гальванопластики для изготовления двумерных решеток, исследованию характеристик фоторезиста, необходимых для технологического процесса, созданию решеток и исследованию их качества с помощью оптической и растровой электронной микроскопии, а также с использованием разработанного алгоритма оценки эффективности решеток в радиографической установке.

В результате исследования были разработаны высококачесвтенные двумерные рентгеновские решетки, а также алгоритм оценки их качества и эффективности.

Разработанные решетки обладают размером 1 см х 1 см, периодом 50, 25, 10 мкм и толщиной от 7 до 32 мкм. Данные решетки готовы к использованию в установках с энергией рентгеновского излучения до 28 кэВ.

Степень реализации: данные проверяются на международных конференциях в Финляндии и Бразилии, а также сообщается на семинарах в Институте

микроструктурной технологии Технологического института Карлсруэ. Рукопись, основанная на полученных результатах, находится в стадии подготовки.

Область применения: медицинская визуализация, характеристика материалов.

В будущем панируется продолжить работу по улучшению характеристик решеток путем использования других составов фоторезистов и рентгеновской литографии для получения структур с высоким аспектным соотношением, которые могут быть использованы при более высоких энергиях рентгеновского излучения. Планируется использовать разработанные решетки в установках рентгеновской визуализации для решения научных проблем в области медицины и материаловедения. С помощью разработанных решеток ожидается значительное улучшение качества получаемых изображений. Кроме того, планируется изучить возможности использования пространственной гармонической однократной съемки с чувствительностью уровня сигнала от малоуглового рассеяния к размеру частиц.

На защиту выносятся следующие положения и результаты:

1) технологический процесс создания двумерных рентгеновских решеток на основе ультрафиолетовой литографии и гальванопластики, обеспечивающий высокую степень периодичности структур;

2) алгоритм оценки качества двумерных решеток и эффективности модуляции ими волнового фронта излучения.

Definitions, designations and abbreviations

phase contrast x-ray imaging (PSI): A group of various technical methods utilizing information concerning changes in the phase of an X-ray beam that passes through an object in order to create its images.

diffraction grating: An optical component with a periodic structure, which splits and diffracts light into several beams travelling in different directions

Talbot-Lau interferometry (TLI): Phase-sensitive X-ray imaging method utilizing three gratings.

single-shot imaging (SSI): Robust x-ray imaging technique which is used to obtain three different and complimentary information i.e. Absorption, Scattering and Phase Contrast from a single exposure of x-rays on a detector.

spatial harmonic imaging (SHI): novel X-ray imaging technique based on Fourier analysis. Also called **spatial frequency heterodyne imaging (SFHI)**.

wavefront modulation (WFM): the X-ray wavefront intensity distribution after sampling by passing through periodic structure which acts a modulating element.

post exposure bake (PEB): photoresist processing step performed before developing, typically to help reduce standing wave phenomena caused by the destructive and constructive interference patterns of the incident light.

Fourier transform (FT): a complex-valued function of frequency, whose absolute value represents the amount of that frequency present in the original function, and whose complex argument is the phase offset of the basic sinusoid in that frequency.

LIGA: a German acronym for Lithographie, Galvanoformung, Abformung (Lithography, Electroplating, and Molding) that describes a fabrication technology used to create high-aspect-ratio microstructures.

ultraviolet (UV): an electromagnetic radiation with a wavelength from 10 nm (30 PHz) to 400 nm (750 THz), shorter than that of visible light but longer than X-rays.

propylene glycol monomethyl ether acetate (PGMEA): a chemical used as a developer to dissolve unexposed negative tone photoresist mr-x 10.

contrast of photoresist: in lithography the development rate as a function of the absorbed light dose.

contrast curve: a plot showing the remaining resist film thickness after development (in relation to the thickness before development) as a function of the (logarithmically plotted) exposure dose. Also called sensitivity curve.

scanning electron microscopy (SEM): a type of electron microscope that produces images of a sample by scanning the surface with a focused beam of electrons.

field of view (FoV): *in optics* a solid angle through which a detector is sensitive to electromagnetic radiation.

reactive-ion etching (RIE): a type of dry etching which uses chemically reactive plasma to remove material deposited on wafers.

polymethylmethacrylate (PMMA): *in microfabrication* positive tone photoresist.

hexamethyldisilazane (HDMS): an organosilicon compound used in microfabrication to improve photoresist adhesion to silicon substrates.

Contents

Introduction

Phase-contrast imaging methods have attracted a lot of attention in the scientific community due to their ability to offer enhanced information about inner structure of the various objects in addition to conventional attenuation contrast. These methods are based on the refraction and scattering of X-rays while passing through the object under investigation. Following the increasing interest, the application of phase-contrast imaging was made available not only at synchrotron facilities with a highly coherent and monochromatic radiation, but also with conventional X-ray tubes [1]. One of the ways to expand the application of phase-contrast imaging is by introducing special optical components, gratings, to the beam path to provide partial coherence of the radiation and improve the resolution of the detecting camera [2]. These methods can be united in the group representing grating-based phase-contrast imaging.

Until recently, among the grating-based imaging methods Talbot-Lau Interferometry (TLI) was one of the most popular approaches to get multi-contrast information on the object structure using not only broad bandpass but also a conventional detector. Despite the evident advantages of the method, there is a trade-off between these benefits and the complexity of the required optical system. Usually TLI exploits three one-dimensional periodic line grating arrangement (source grating, phase grating and absorption grating), where phase grating and absorption grating in front of the detector must be well aligned to detect small distortions of the X-ray wave front generated by the object under investigation [3]. Together with sophisticated stepping procedure, which requires extremely stable and precise controlling system and several X-ray exposures, these characteristics impose a certain difficulty on the measurement procedure. Additionally, one-dimensional line gratings allow only orientation-dependent analysis of structures, because they are only sensitive in the direction, perpendicular to the grating lamellas [4].

Responding to the need for orientation-independent characterization within simplified setup and fewer requirements on grating quality non-interferometric wave front sensing methods have been proposed recently [5-7]. These methods can operate with broadband radiation, do not require stepping procedure and thus can be applied for single-shot imaging. A single-shot setup configuration, apart from micro focus X-ray tube and X-ray camera, includes a unique two-dimensional grating to provide with enhanced information on material structure in several directions ensuring thorough characterization of the object under investigation. In this approach the incident beam is periodically modulated by an absorption grating, and the distortion of the regular pattern introduced by

the object is recorded with single exposure and then analyzed. There are several data processing algorithms on how to retrieve three contrast modalities from the grating-object image projected on the detector. One of these algorithms is based on the *spatial harmonic imaging* approach (or it's modification – *spatial frequency heterodyne imaging*) [6-12], where the image at the detector, which is the convolution of the object and the grating images, is Fourier-transformed into a spatial frequency spectrum. This spectrum is the sum of a series of harmonic spectra that can be separated to yield all three contrast modalities. Spatial frequency harmonic imaging has been successfully implemented for medical imaging [6, 9-10], materials science [11-12], and also was adapted for soft X-rays [8].

Considering the growing interest to the single-shot imaging methods which require two-dimensional gratings it is consequential to draw attention to the optical components in use. Gratings for X-ray imaging are represented by the matrix with periodically alternating opaque and transparent structures to either effectively absorb or transmit X-ray radiation respectively (figure 1). As in the abovementioned methods information is retrieved from the overlapped grating-object image, it is of great importance to insure high quality and efficient performance, as it was emphasized in [8], that using gratings of greater symmetry may increase the efficiency of sampling of Fourier spectra. Thus, higher degree of periodicity of the grating structures can increase the quality of the final image, thus it is necessary to remove or at least reduce to the minimum the amount of irregularities in the grating pattern, which can be falsely treated during data processing as the distortions introduced by the object. It is also important to keep in mind that the resolution of the final image in a single-shot approach is defined by the period of the grating [6, 8], although to avoid overlapping of the harmonics, the camera pixel size should be less than projected grating period divided by 3 [6]. Thus the optimal grating period is an open question, which corresponds to the available X-ray camera and X-ray source: the grating period should be as small as possible to ensure sufficient final image resolution, but large enough to meet the mentioned criterion.

Sufficient wavefront modulation is another characteristic that directly influences the contrast of the image acquired by the detector. Here by the efficiency of wave front modulation (WFM) we mean the signal intensity variation recorded by the camera. It can be expressed similarly to the visibility characteristic used in TLI [13]:

$$WFM = \frac{I_t - I_{op}}{I_t + I_{op}},$$

where I_t – intensity, transmitted by the transparent structure, I_{op} – intensity, transmitted by the opaque structure. In theory, I_{op} = 0 and $I_t = I_0$, where I_0 is the intensity of the X-rays incident upon the grating, thus the WFM should always be equal to unity. Although in reality it is not always the case as for a certain grating at lower energies highly transmitting structures can be slightly absorbing and at higher energies the opaque material will transmit some radiation.

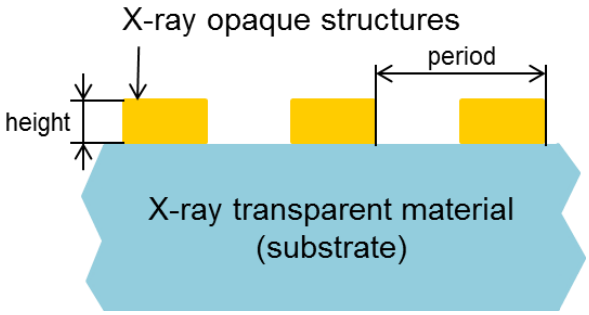

Figure 1 – Schematic drawing of the grating

Different periodic structures were mainly used before for single-shot imaging applications such as different commercially available metal meshes: Bucky grid (lead and aluminum) [6], Nickel wire mesh [8, 9], stainless steel mesh [11], although there were examples where gold grating of 30 μm electroplated on 100 μm glass substrate were utilized at the energy of 50 keV [14]. Albeit gold absorbs X-rays much more efficiently than nickel and stainless steel, the height of 30μm only stops about 35 % of incident radiation, leading to WFM = 0.2. This may lead to the decreased contrast of the final images.

To explore the possibilities of the spatial frequency harmonic imaging and single-shot imaging approach in general it is important to achieve highest wavefront modulation keeping high degree of periodicity for the gratings in use. In this regard the objective of this work is *to develop high quality gratings of various periods and with intended structure height suitable for X-ray energy to be used in the single-shot imaging setup*. To achieve abovementioned objective it is required to accomplish the following tasks:

a) to establish technological process for development of two-dimensional X-ray gratings;

b) to manufacture the gratings testing different layouts and tailoring for single-shot imaging;

c) to optimize the fabrication process based on acquired information;

d) to evaluate the quality of the final gratings with scanning electron microscopy;

e) to develop an algorithm for evaluation of grating performance in a sing-shot configuration;

d) to evaluate and test two-dimensional gratings in the single-shot imaging configuration.

The following theses and results are subjected to defense:

1) the technological process of fabrication of two-dimensional X-ray gratings based on ultraviolet lithography and gold electroforming, ensuring a high degree of periodicity of structures;

2) algorithm for estimation of the two-dimensional gratings quality and the efficiency of the wavefront modulation caused by the grating.

Chapter 1 Grating-based X-ray imaging

Nowadays the vast majority of X-ray imaging techniques are based on the absorption of the radiation by the object, where the information is given by the difference in the attenuation coefficient of the object constituents. However, another approach has been used extensively in light microscopy – phase contrast imaging, which relies on differences in the refractive index of different materials. This approach was extended to X-rays, although for this kind of radiation the changes in refractive index are minor and require special methodology and equipment to detect them [1]. When X-rays are passing through the materials, they undergo refraction on the edges and interfaces giving the information on changes in the phase. Another advantageous type of contrast first applied in light microscopy and later to X-rays as well is diffraction contrast (small-angle scattering or dark-field contrast). It arises from scattering of the X-rays on micro- and nanostructures, which are smaller than diffraction limit and result in fringes which cannot be directly resolved by the X-ray camera [2,3] These two additional types of contrast can reveal essential mesoscopic and microscopic properties of the object (figure 2). Along with the development of coherent X-ray synchrotron sources, several types of dark-field and phase contrast methods were developed for synchrotron X-ray imaging and tomography. Several techniques have been studied for phase-sensitive imaging, e.g. propagation-based phase contrast and diffraction-enhanced imaging. These techniques need a coherent X-ray radiation with high flux, such as synchrotron radiation facilities.

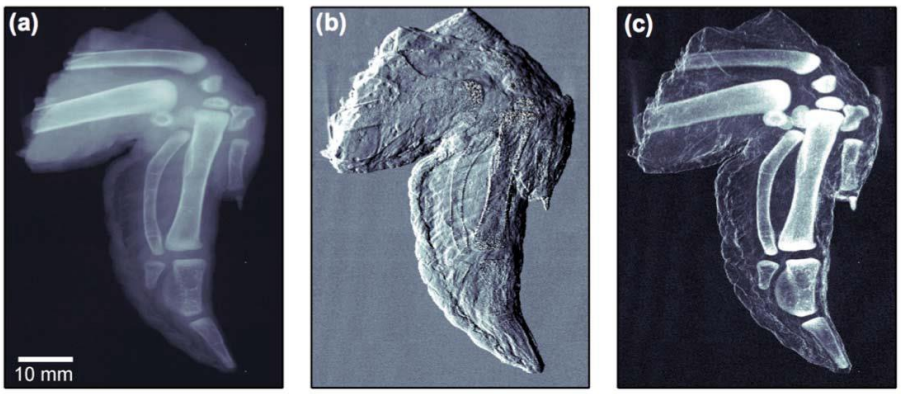

Figure 2 – Demonstration of three X-ray contrast modalities obtained for a biological specimen (a chicken wing): a) absorption, b) differential phase and c) small-angle scattering or dark-field [2]

However, the complexity of synchrotron sources and the need of elaborate optical elements limit the accessibility of the techniques and also increase the operational costs. The other group of scattering- and phase-sensitive imaging techniques was developed primarily to allow such measurements on lab-scale, using e.g. the conventional X-ray tubes as the radiation sources. The grating-based techniques proved to be robust, scalable and already found their practical applications in X-ray imaging.

1.1 Talbot-Lau Interferometry

Talbot-Lau Interferometry (TLI) is the most popular phase-contrast imaging method, as it overcomes the limitation imposed by the use of synchrotrons [16]. It offers multimodal information based on absorption, small-angle scattering and phase contrast. The increase of information can highly improve sensitivity and specificity for various investigations.

The TLI system utilizes a set of three one-dimensional gratings arrangement between the incoherent radiation X-ray source and the X-ray detector (figure 3 *a*). The arrangement includes source grating, which is placed right after the X-ray source and serves to provide sufficient coherence of radiation. The source gratings consist of periodical slits to generate an array of line sources. The phase grating introduces phase shift by beam splitting due to diffraction (figure 3 *b*). The grating is placed before or after the object, depending on a specific setup configuration. Usually the period of the phase grating is smaller than detector pixel size (few μm), thus to resolve generated fringes the analyzer grating (or absorption grating) should be introduced. Analyzer grating consists of strongly absorbing lines and acts as a transmission mask for the detector, thus should be placed in front of the detector. The gratings must be well aligned to detect small distortions

of the X-ray wave front generated by the object under investigation [3]. Furthermore, the spatial resolution of the TLI is restricted by the challenge of fabricating high aspect ratio one-dimensional gratings with periods smaller than 2.4 μm [17].

To align the gratings and to perform stepping curve (figure 3 *c*), which is required in order to resolve phase grating pattern by conventional detector, highly stable and precise mechanical system is necessary, which makes image acquisition a complex and time-consuming procedure. In addition, one-dimensional gratings allow only orientation-dependent analysis of structures, because they are only sensitive in the direction, perpendicular to the grating lamellas [18]. Radiographic imaging is widely used to study dynamic processes, but the orientation dependency in this case result in insufficient information about the inner structure of the object. Fully two dimensional information can only be acquired by two-directional scanning [18] or utilizing two-dimensional optical components [19]. The lack of imaging information in direction parallel to the grating lines has been reported as well for other X-ray imaging modalities [20].

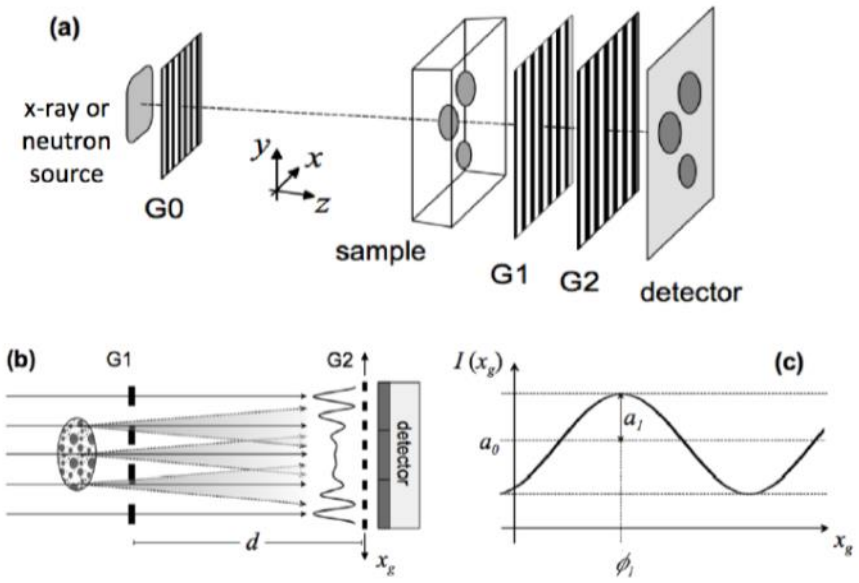

Figure 3 – *a*) Setup with a source grating G0, a phase grating G1, and an analyzer absorption grating G2. *b*) Through the Talbot effect a linear periodic fringe pattern is created behind G1 in the plane of G2. *c*) Intensity modulation detected in a detector pixel when one of the gratings is scanned along x_g. A detailed analysis of the sample-influenced shape of the curve yields transmission, phase-contrast, and dark-field/scattering images [21]

Talbot-Lau interferometry has been successfully implemented for medical imaging [18, 22] and material science applications [23, 24] within laboratory setups, providing quantitative information and high contrast. Although in the recent years, responding to the need of decreasing the X-ray dose to the medical specimens [25] and investigation of

dynamic changes in the sample (e.g. phase transitions [11]), prompt and robust multi-contrast X-ray imaging techniques have been proposed, which can obtain all three contrast via a single projection.

1.2 Single-shot imaging with a single optical element

All single shot grating-based X-ray imaging setups have similar basic approach beneath them: to modify a conventional radiography setup to acquire three type of contrast via a single projection. In a single-shot configuration usually a single grating introduced usually between the X-ray tube and the object in order to reduce the dose to the sample [9, 14]. However, setup arrangement with object placed before the grating is used as well [6, 12]. All the methods use the grating-only image with no object in the beam path as a reference to clear the acquired images and eliminate the imaging setup impact to the final image (X-ray source radiation inhomogeneity, initial defects of the grating, dead pixels of the detector, etc.). In the following measurement grating pattern distorted by the object is projected onto the detector and recorded to be subsequently analyzed. The difference in overlapped image processing divides the method into three approaches:

a) **Local method (correlation analysis):** the grating distortions are resolved into horizontal and vertical components directly by the detector with high spatial resolution [5];

b) **Intensity distribution method (subpixel resolution analysis):** the method is based on precise subpixel position determination of the X-ray pattern projected by the grating directly from the pattern image. Microfocus tube and a high spatial resolution detector (e.g. hybrid semiconductor pixel detector) are required [14, 26];

c) **Fourier analysis (spatial harmonic imaging and spatial frequency heterodyne imaging):** there are two treatments of this approach – apply Takeda's method [27] of Fourier analysis [6, 10] and using a modified hybrid input-output algorithm based on heterodyning effect given by the grating [7-12]. Both approaches apply Fourier analysis and consequent synthesis to the recorded projected image.

1.2.1 Correlation analysis of local shifts in intensity

A single-exposure quantitative method of X-ray phase contrast imaging based on correlation method of local intensity shifts was proposed by *Morgan et al.* [5]. The gist of the method is analyzing how a high visibility reference grid pattern is deformed by the presence of the sample by resolving the pattern into horizontal and vertical components (figure 4). Unlike methods based on Takeda's method of Fourier analysis, sample size

here can be very small relative to the grating period and smaller than the Field of View (FoV) of the setup.

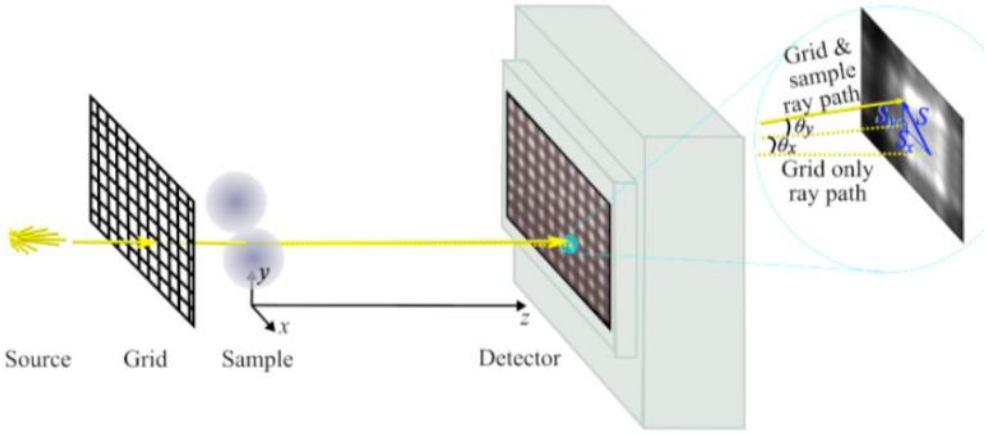

Figure 4 – Experimental setup for quantitative single-exposure x-ray phase contrast imaging using a single attenuation grating to perform correlation analysis of local shifts in intensity [5]

The method compares the grating-sample image with a reference grating-only image taken separately, and then reference pattern shift *S* is determined for each pixel, utilizing real-space analysis. The closest correlation between grating-only and grating-sample patterns is found and resolved into horizontal S_x and S_y vertical components (figure 5). Plotting of these shifts gives a differential phase contrast images in two directions, giving quantitative information about the phase shift. From these images projected thickness map can be reconstructed.

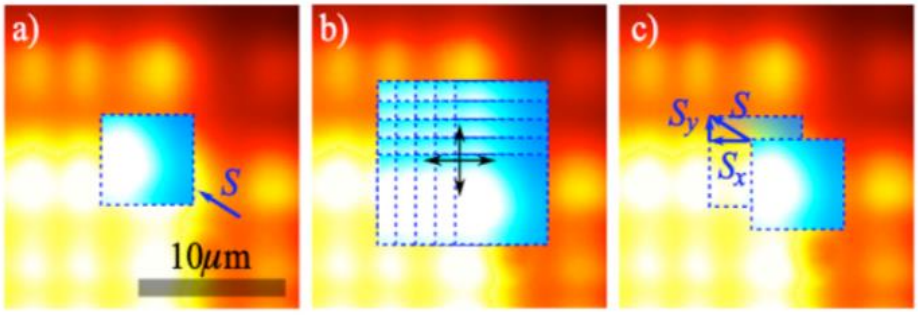

Figure 5 – Scheme the cell of cross-correlation shift alignment of the grating only (red) and grating-object (blue). This procedure is repeated for each coordinate of grating-object image [5]

The method thus provides quantitative information about phase contrast, but it doesn't provide with simultaneously acquired absorption and small-angle scattering images. The method is not sensitive to the grating quality and can utilize a random phase optical component (e.g. paper [28]). Although it should be possible to use this method with table-top X-ray sources, it has only been implemented using a synchrotron radiation with high spatial resolution detectors (pixel size around 0.18 μm) [5].

1.2.2 Subpixel resolution analysis of intensity distribution

Subpixel resolution analysis is based on a similar approach as local method: the grating-only image signal is compared to the grating-object signal, but here the distortions introduced by the object are analyzed with subpixel resolution. Intensity distribution of the beamlets formed by the mesh grating is weighted by recording grating-only image. After the object is placed on the beam path, refraction shift occurs within it, and the phase shift is calculated by estimating the ratio of intensity distribution between adjacent pixels.

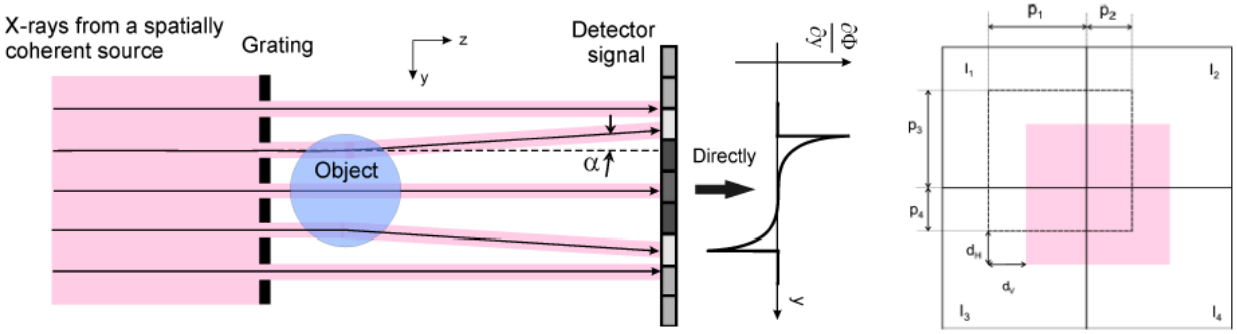

Figure 6 – *a)* Setup scheme for single absorption phase-contrast technique, where the phase gradient is calculated directly from the detector signal; *b)* position of the original (dashed) and refracted (pink) beam. The non-symmetrical initial beam alignment is more convenient for practical measurements [14]

As the phase gradient is obtained directly from the detector signal (figure 6 *a*), calculation of the values are quite straight-forward. Labeling the intensity in the respective neighboring four pixels I_1', I_2', I_3', I_4' in the case without the object and I_1, I_2, I_3 and I_4 in the case with the object (figure 6 *b*), then the horizontal shift d_H, vertical shift d_V and attenuation image A can be calculated as:

$$d_H = p_1\left(\frac{I_1}{I_2}-\frac{I_2'}{I_1'}\right)\cdot\left(1+\frac{I_1}{I_2}\right)^{-1},\ d_V = p_3\left(\frac{I_1}{I_3}-\frac{I_3'}{I_1'}\right)\cdot\left(1+\frac{I_1}{I_3}\right)^{-1},\ A=\frac{I_1+I_2+I_3+I_4}{I_1'+I_2'+I_3'+I_4'}. \quad (1)$$

Subpixel analysis of intensity distribution requires high spatial coherency of the source (micro- or even nanofocus tube) to give well-defined beamlets and as it is clear from its name, detector with high spatial resolution is the base of this approach (e.g. Medipix2 detector). The method has been applied for high energies (70 keV) [26] and allows obtaining absorption and phasing images simultaneously from a single projection. Although as the previous method Subpixel analysis cannot be applied to acquire small-angle scattering signal.

1.2.3 Spatial harmonic frequency methods and their application

1.2.3.1 Spatial Harmonic Imaging

The Spatial Harmonic Imaging (SHI) utilizes Takeda's fringe pattern analysis and was first introduced for single-shot imaging by *Wen el al* [20]. It is based on a Fourier satellite approach analysis of a projected image. By this method a raw image, consisting of the overlay of the grating pattern and the object, is converted using discrete Fourier transformation (FT) into its spatial frequency spectrum in the Fourier domain. Fourier transform of the raw image contains a primary peak at the center, which is not affected by diffraction, and harmonic peaks corresponding to the periodicity of the gratings. The spatial frequency content of the sample projection image is duplicated at each peak, which provides a harmonic spectrum. If the harmonic spectra do not overlap, the inverse Fourier transformation of a sub-region centered at a peak yields corresponding primary and harmonic images. The ratio between the two is a scattering image (figure 7). Phase-contrast image is obtained by mapping the shifts of first order harmonic relative to the grating-only image. In the figure 7 one-dimensional case is shown, which is easily extended for two-dimensional case where two Fourier spectra will be obtained in two directions sharing zeroth order harmonic.

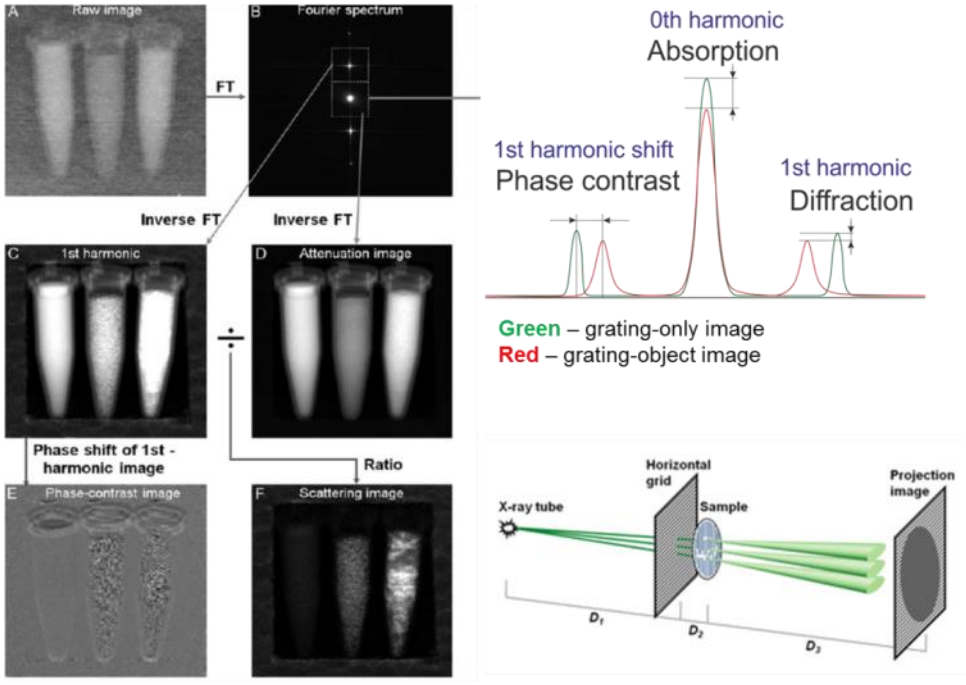

Figure 7 – Illustration of spatial harmonic method for single-shot imaging in one-dimensional case (for simplicity). The raw image is Fourier transformed into a spatial frequency domain forming a spectrum. Harmonics of the spectrum are inverse Fourier transformed separately to yield three contrast modalities via single image (adapted from [20])

Spatial Harmonic method has been extended to obtain differential phase information by using two-dimensional transmission gratings and successfully implemented

at energy of 27 keV for medical imaging [6]. Example of images acquired with SHI for medical imaging is shown in figure 8. Even though the resolution of phase and absorption contrast images is limited by gratings density and camera pixel size [30], it has impressive potential for acquiring specific spatial information from small-angle scattering contrast. This fact deserves a special attention from the point of view of characterization at sub-μm as small-angle scattering signal originates from the variations of the electron density at the nanoscale.

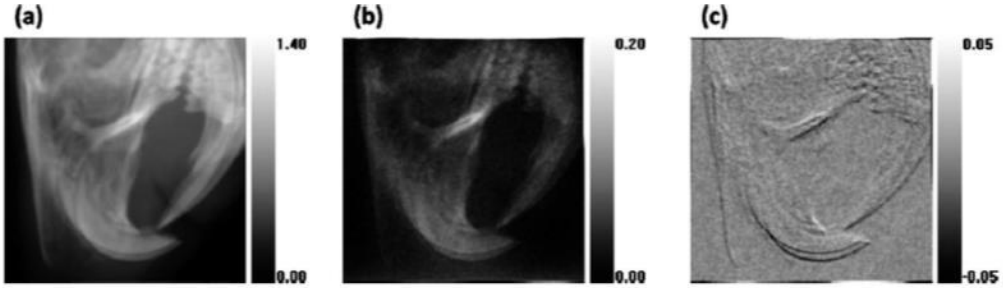

Figure 8 – Single-shot SHI of mouse snout taken *ex vivo* a) absorption image, b) diffraction image, c) differential phase-contrast image [30]

Following the development of spatial harmonic imaging, the diffraction effect was quantified in terms of the sample's material complex refractive index in a grating-before-sample geometry with the first principle calculations. Scattering signal selectivity associated with particle-size sensitivity was theoretically predicted and supported by measurements at a synchrotron using microsphere suspension as a test sample. It was proven that for specific auto-correlation lengths associated with scatterer size the diffraction signal significantly increases. In addition to measurements at the synchrotron, 3D tomography measurements of iron-oxide nanoparticle suspension with particle sizes varied from 100 to 200 nm and potassium iodide (KI) solution were performed at 30 keV [31]. The measurements were conducted under setup arrangement providing auto-correlation length of 160 nm, thus enabling sensitivity to the features of the same size.

To demonstrate selective diffraction imaging for a relevant application and to differentiate between particles of different sizes, iron-oxide nanoparticles and potassium iodide solution had been implemented into a bone structure of a chicken wing and visualized using the abovementioned approach [32]. Selectivity in this case was performed by placing two one-dimensional line gratings perpendicular to each other at fixed distances A and B from the object (see figure 9 *a*) in order to record two images for different grating-object distances (and different scattering lengths respectively) via a single exposure. The absorption image (figure 9 *b*) was used as a reference to detect the presence of particles. In the absorption image injected particles as well as surrounding tissue are clearly visible. To perform selectivity the ratio between two diffraction images (figure 9 *c*) from both

gratings was plotted, demonstrating scattering impact of iron oxide particles only as the scattering length for the setup was 87 nm, which corresponds to the iron oxide particles sizes.

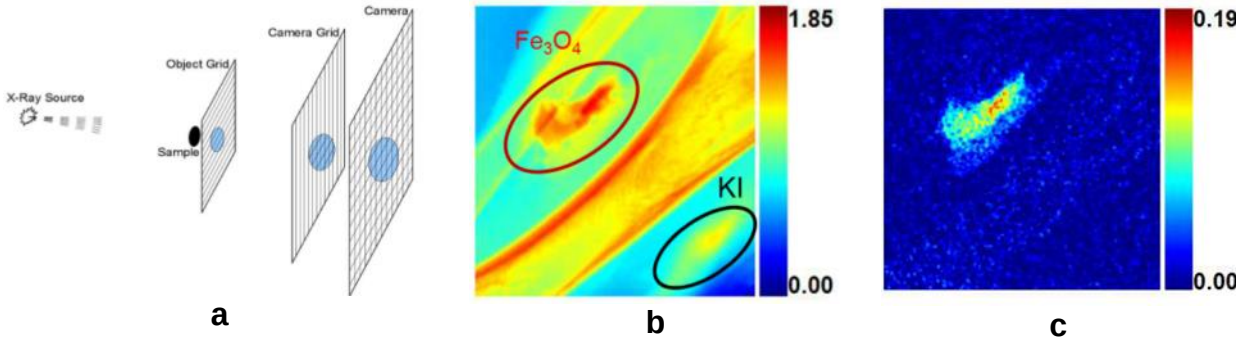

Figure 9 – *a)* The double-grating setup for selective diffraction imaging *b)* absorption image of a chicken wing injected with iron oxide particles (red oval) and potassium iodide (black oval) *c)* double-grating diffraction image visualizing the presence of particles with the sizes less than 87 nm [32]

1.2.3.2 Spatial frequency heterodyning imaging

Another interpretation of the SHI was formulated by the group of *Rose-Petruck*. In the work of *Wu et al* [7] it was shown that the placement of the grating adjacent to the object results in spatial heterodyning of the phase and absorption features of the object that is a spatial analogue of the time domain heterodyning used in radio electronics. Spatial frequency heterodyning imaging (SFHI) relies on the effect of a “local oscillator” in the spatial frequency space of the X-ray image of an object. This local oscillator is produced by imaging an object with a superposed transmission grating. Mathematical cross-terms between the local oscillator’s and object’s spatial frequencies result in image contrast enhancement [8].

The procedure of spatial harmonic analysis consists of three consecutive steps (figure 10): 1) Fourier Analysis – forward FT of the real grating-only and grating-object images yielding the complex spatial frequency spectra; 2) Fourier synthesis – the inverse FT of the selected (zeroth and first) components of the spatial frequency spectra yielding the complex zero and first order components of the image; 3) Algebraic manipulation of the individual complex components to obtain the desired contrast image (absorption, phase and scattering contrasts). Using a two-dimensional grating 2D discrete FT can be applied of the acquired images. The SFHI analysis then yields the pair of grating deflection images and scattering images of the sample. The images express the amount of deflection/scattering in the direction perpendicular to the grating’s lamellas. The decomposition of the Fourier spectra of the image into 0^{th} and 1^{st} order harmonics requires

a band-limited image. The spectra overlap of the adjacent spectral components can be averted by ensuring that the frequency of the grating's intensity is at least twice the maximal frequency component in the object image [29].

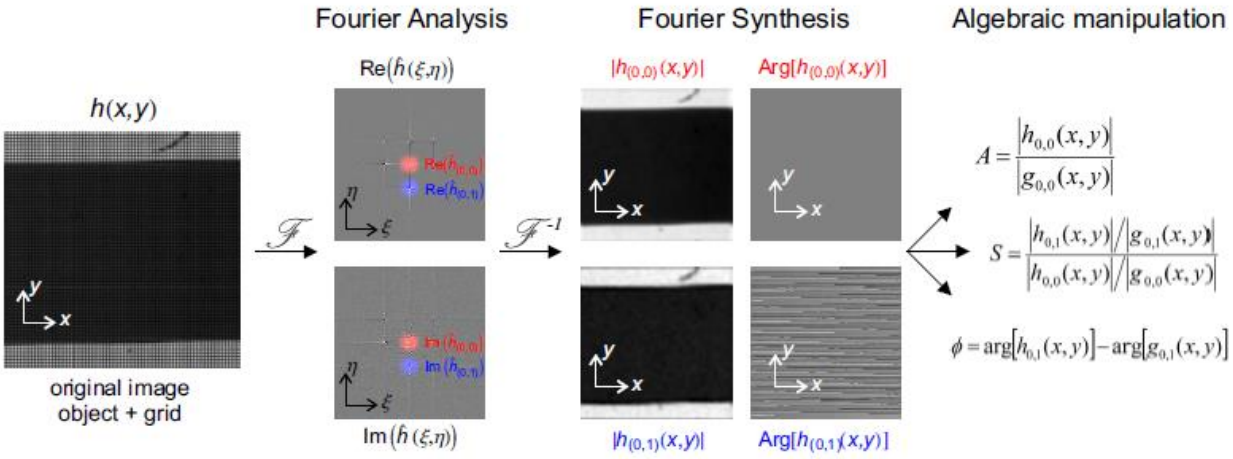

Figure 10 – The fundamental processes of the discrete two-dimensional spatial harmonic analysis [20], performed on the image of the grid with object h(x; y). A complementary analysis of the image of the grid alone g(x; y) is not shown [29]

SFHI doesn't have strong requirements on spatial coherency of the source, thus common X-ray tube can be used. SFHI has been successfully implemented at X-ray energies around 30-50 keV for imaging of hepatocellular carcinoma in a mouse model [9-10] (figure 11).

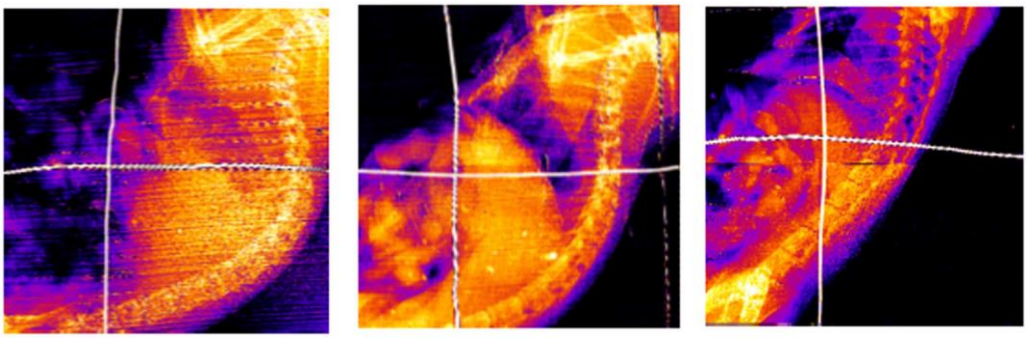

Figure 11 – X-ray scatter images of mice 48 hours after receiving injections of saline (left), 50 nm Au-based nanoparticles (AuNPs) of different composition (middle and right). The crossed wires mark the position of the liver, which should take up significant amounts of AuNPs due to the phagocytic ability of macrophages in the liver [9]

Time-resolved studies were conducted to describe aqueous phase transitions inside multi-walled carbon nanotubes (MWCNT) [11]. Evaporation and condensation of water on MWCNT surfaces were studied as a function of time and temperature and correlated to the shape of scatter profiles and contained water volume (figure 12).

The characterization technique itself was adapted for a new spectral range – soft X-rays [8, 29]. In the figure 13 one can see images acquired with a dried cryo-microtome slice of tendon with absorption, directional scattering and phase contrasts. In the work of

Bruza [8] it was specifically underlined that using gratings of greater symmetry may increase the efficiency of sampling of Fourier spectra.

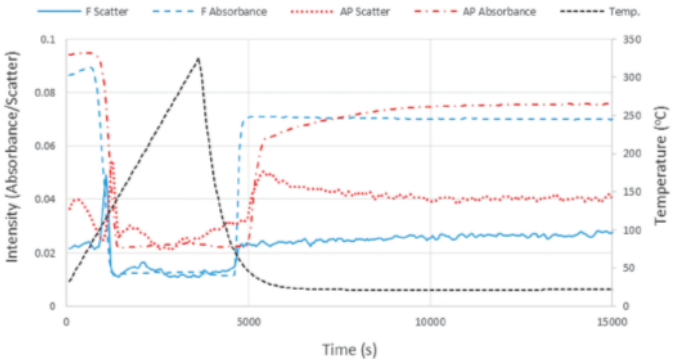

a

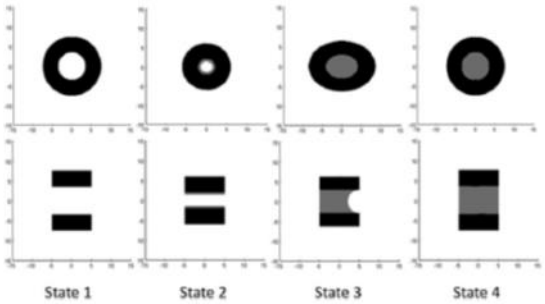

b

Figure 12 – *a)* A one hour heating ramp to 320 °C and subsequent cooling period were applied to the samples. F and AP stand for functionalized by oxidation and as-purchased respectively; *b)* Demonstration of phase stated of MWCNT from empty CNT with circular cross section (state 1) with contracted transitions partially filled with eater (state 2 and state 3) to original cross section and complete filling with a planar menisci at both ends (state 4)

Single-shot imaging is a prompt and robust visualization technique which has already been implemented for various applications. It has a potential for directional and size-sensitive scattering signal separation to perform selective imaging. For further development and improvement of the resolution and image quality intended optical elements such as diffraction gratings need to be manufactured providing with homogeneous and efficient wavefront sampling.

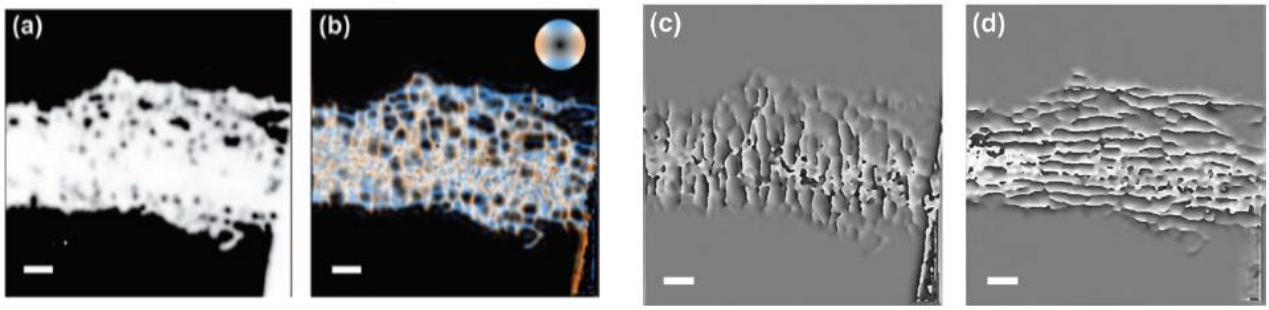

Figure 13 – Soft X-ray SFHI of a dried cryo-microtome slice of tendon: *a)* absorbance image *b)* SFH image of the directional scattering; *c)* and *d)* are the (1,0) and (0,1) orders of the differential phase contrast images. Scale bar 100 μm [8]

1.3 Requirements imposed on gratings by Single-Shot Imaging

As in the abovementioned methods information is retrieved from the overlapped grating-object image, it is of great importance to insure high quality and efficient performance, as it was emphasized in [8], that using gratings of greater symmetry may increase the efficiency of sampling of Fourier spectra. Thus, higher degree of periodicity of the grating structures can increase the quality of the final image, therefore it is necessary

to remove or at least reduce to the minimum the amount irregularities in the grating pattern, which can be falsely treated during data processing as the distortions introduced by the object. It is also important to keep in mind that the resolution of the final image in single-shot approach is defined by the period of the grating [6, 8], although to avoid overlapping of the harmonics the camera pixel size should be less than the projected grating period divided by 3 [6]. Thus the optimal grating period is an open question, which corresponds to the available X-ray camera and X-ray source: the grating period should be as small as possible to ensure sufficient final image resolution, but large enough to meet the mentioned criterion.

To evaluate the quality of the gratings it is necessary to study the wavefront sampling induced by the two-dimensional transmission gratings. Efficiency of wavefront modulation of X-rays by diffraction grating is defined by:

- period of the gratings in two dimensions;
- height of absorbing structures;
- transmittance of the supporting substrate;
- homogeneity of the gratings structures in height distribution and periodicity.

These parameters should ensure clear modulation of the wavefront; ideally the absorbing structures should absorb 100 % of incident X-ray radiation and the supporting wafer (substrate) – 0 % of radiation meaning complete transparency. The grate pattern should be regular within the whole grating area. Principle of wavefront sampling by two-dimensional transmission grating is represented in figure 14.

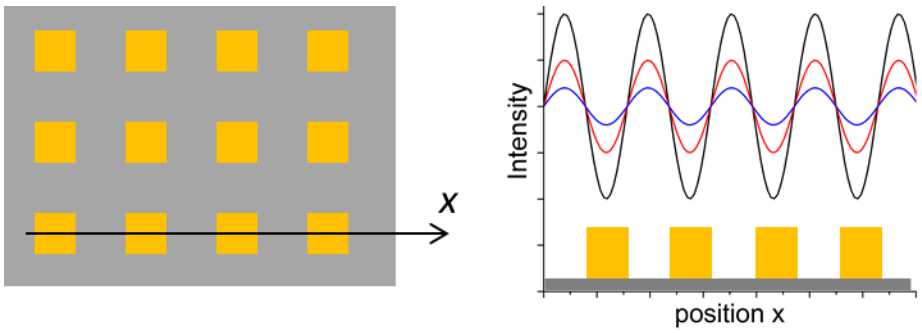

Figure 14 – Principle of wavefront sampling by two-dimensional transmission grating: *a)* two-dimensional grating pattern, *b)* one dimensional intensity distribution in a certain beam section after the grating: black line stands for highly efficient modulation, red for intermediate efficiency and blue for a weak wavefront modulation

Two-dimensional grating is represented by the matrix/stencil with periodically alternating opaque and transparent structures (figure 14 *a*). When X-ray radiation is incident on the grating, part of it is transmitted by the low-absorbing substrate (attenuation should be less than 5 %), while radiation incident on the gold structures array is almost

completely absorbed (90 % absorption and higher). Diffraction on the multiple apertures occurs, but its effect is very weak due to short wavelengths of X-rays. All this effects combined form multiple coherent point sources and wavefront is sampled to create a pattern inverse to the grating. Intensity distribution in a certain beam section after the grating is shown in the figure 14 *b*. The black line indicates the most efficient wavefront modulation, as one can see it has sinusoidal distribution. In figure 14 *b* blue line represent very weak one, which will result in low contrast of the final images during measurements. Thus one can conclude that the amplitude and periodicity of the wavefront modulation (X-ray beam intensity distribution) define the efficiency of the wavefront sampling by the transmission grating.

Sufficient wave front modulation can also be expressed similarly to the visibility characteristic used in TLI [13]:

$$WFM = \frac{I_t - I_{op}}{I_t + I_{op}}, \tag{2}$$

where I_t – intensity, transmitted by the transparent structure,

I_{op} – intensity, transmitted by the opaque structure.

In theory, $I_{op} = 0$ and $I_t = I_0$, where I_0 is the intensity of the X-rays incident upon the grating, thus the WFM should always be equal to unity. Although in reality it is not always the case as for a certain grating at lower energies highly transmitting structures can be slightly absorbing and at higher energies the opaque material will transmit some radiation.

Different periodic structures were mainly used before for single-shot imaging applications such as different commercially available metal meshes: Bucky grid (lead and aluminum) for SHI [6], Nickel wire mesh [8, 9] and stainless steel mesh [11] for SFHI, although there were examples where gold grating of 30 μm electroplated on 100 μm glass substrate were utilized at the energy of 50 keV for subpixel resolution analysis of intensity distribution [14]. Albeit gold absorbs X-rays much more efficiently than nickel and stainless steel, the height of 30 μm only stops about 35 % of incident radiation, leading to WFM = 0.2. This may lead to the decreased contrast of the final images. To explore the possibilities of the spatial frequency harmonic imaging and single-shot imaging approach in general it is important to achieve highest wavefront modulation keeping high degree of periodicity for the gratings in use.

Chapter 2 Grating patterning technology

2.1 UV LIGA for X-ray grating fabrication

LIGA is a German acronym for Lithographie, Galvanoformung, Abformung (Lithography, Electroplating, and Molding) that describes a fabrication technology used to create high-aspect-ratio microstructures. There are two main LIGA-fabrication technologies, X-Ray LIGA, which uses X-rays produced by a synchrotron to create high-aspect ratio structures, and UV LIGA, a more accessible method which uses ultraviolet light to create structures with relatively low aspect ratios when compared with X-ray lithography.

Ultraviolet lithography (UV lithography, photolithography) is a patterning technology that transfers a pattern from a mask to a photosensitive polymer (photoresist) layer by using a standard lithographic process with the exposure of the photoresist by ultraviolet radiation. Photolithography employs a UV light source, an optical system, a mask, and a photoresist film coating the surface of a substrate into which a desired pattern is to be transferred (figure 15). Photolithography is widely used in microelectronics for the fabrication of transistors on a silicon substrate; however, this technology can also be used as a tool for creating diffraction gratings for energies below 40 keV. In this case, the required height of the final structures does not exceed 25 μm [33].

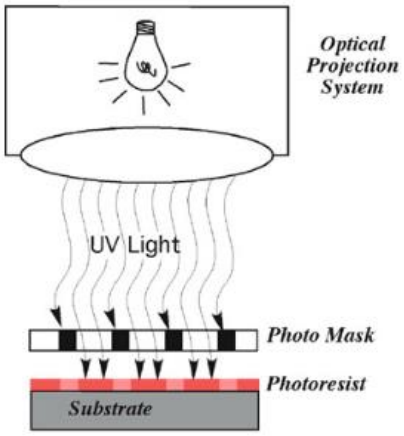

Figure 15 – Scheme of photolithography setup, consisting of UV lamp, optical projection system, photomask and a substrate with photoresist layer [34]

Lithography is a sequence of photochemical processes that creates on the surface of the material a protective layer of the required configuration, thickness and resistance to aggressive processes such as subsequent selective ion etching or metal electroforming using cross-linked photoresist pattern. Optical lithography uses ultraviolet (UV) radiation

with a wavelength of λ = 310-450 nm to expose the photoresist: by light (*photo*) in a stone (*lithos*) draw (*grapho*).

The lithography process uses a mask comprised of altering transparent and opaque regions laid out to form a pattern. Typically the plate is either glass or quartz that has been designed for transparency in the UV and contains an opaque patterned metal film such as a typical 800 Å thick chromium layer on the top surface. Photomasks can be designed for either clear field or dark field patterning. A dark field mask has the desired pattern contained in the transparent part of the mask whereas the clear field mask has the pattern contained in the opaque part of the mask.

Using an optical projection system, mask pattern is illuminated onto a photosensitive film called a photoresist. Depending on the optical projection system, contact, soft-contact, and proximity alignments can be performed to produce a 1:1 image in the photoresist layer:

a) contact aligner: photoresist is in intimate contact with the chrome-side of the mask at the time of exposure. Mask image is 1:1, in theory is not limited by diffraction (figure 16 *a*);

b) proximity aligner: photoresist is not in intimate contact with mask – separated by a few microns. Mask image is 1:1. Usually is used in order not to prevent soiling the mask surface, limited by near field (Fresnel) diffraction (figure 16 *b*);

c) projection aligner: photoresist is not in intimate contact with mask – mask image is projected onto resist by lenses, limited by far field (Fraunhofer) diffraction.

Projection alignment requires a complex optic system in order to provide different mask to the resist pattern ratios. This alignment mode is not relevant for grating fabrication, since it provides with Gaussian light intensity profile shape (figure 16 *c*).

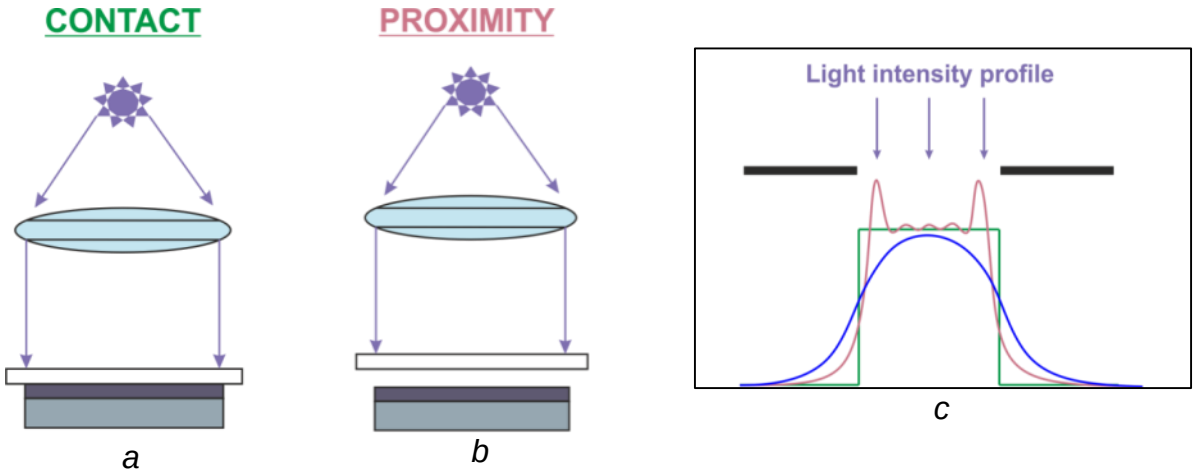

Figure 16 – Lithography setup alignment modes suitable for grating fabrication: *a)* contact alignment, *b)* proximity alignment, *c)* intensity profile for contact mode (green), proximity mode (pink) and projection mode (blue). Based on Ref. 35

When light strikes the photoresist, it undergoes a chemical change which in turn changes the ability of the photoresist to be dissolved by various solvents. This allows specific areas of the photoresist layer to be removed, which creates a pattern on the substrate surface, which can be used as a stencil for consecutive metal electroforming.

Metal electroplating for transmission gratings is usually performed using gold as it efficiently attenuates X-ray radiation. Electroplating bath represents an electrolytic cell where a cathode represents a wafer with photoresist pattern to be plated. Gold is plated upward from the metalized substrate into the voids left by the removed photoresist in the electroplating bath environment.

Summarizing above-mentioned process details, the lithographic process of grating fabrication can be divided into three main steps, each of which includes a series of sequentially performed operations (figure 17).

Step 1. Formation of a continuous uniform layer of resist on the surface of the substrate (usually performed by spin-coating):

a) preparation of the substrate surface (e.g. prebake, plasma etching, application of adhesion promoter);
b) application of a photoresist layer (spin-coating);
c) drying of the resist (soft bake after spin-coating).

Step 2. Create a photoresist pattern structure (direct or inverse mask pattern):

a) exposure with UV light;
b) post exposure bake;
c) development of photoresist;

Step 3. Transfer of the photoresist pattern to the absorbing pattern (e.g. gold structures):

d) etching of the photoresist layer to ensure clear gold pattern formation;
e) electrodeposition of gold;
f) removal of the resistive mask (optional).

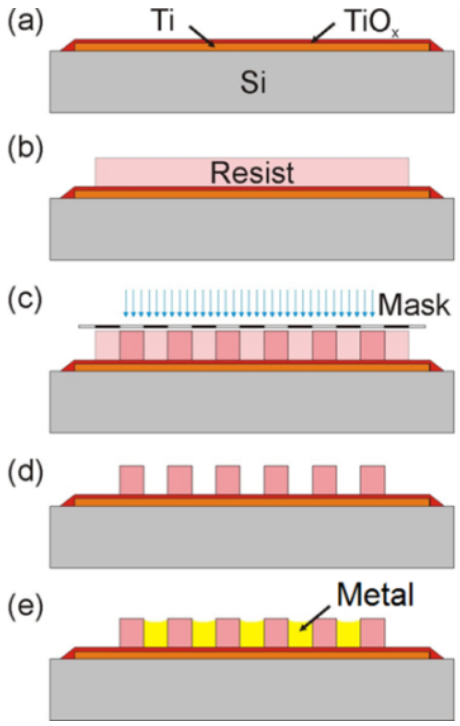

Figure 17 – UV LIGA process for grating fabrication

UV lithography is one of the most available and widely used microstructure fabrication techniques for patterning of periodic structures. UV lithography can provide with high quality structures, if the technological process is optimized for required structure size considering that diffraction limits the patterning resolution. The main parameter to optimize is the exposure surface energy, as radiation distribution is influenced by the diffraction.

2.2 Photoresist and its characterization

Photoresist typically consists of a mixture of organic polymers in a solvent combined with photosensitive additives. Photoresist is designed to change solubility due to exposure to UV light. The exposed area becomes either more soluble (positive photoresist) or less soluble (negative photoresist) upon exposure. The difference between these two main types of photoresist chemistries (positive and negative photoresist) is not only the pattern itself, but also the edge profile resulting from absorption of UV light during exposure, which is illustrated in a figure 18. Due to absorption affects, the top surface of the photoresist receives a larger exposure dose than the bottom surface. This results in a slightly larger exposed area at the top surface as compared to the bottom surface. This means that more material will be dissolved away more either at the top or at the bottom. For a positive photoresist, such an exposure profile versus depth results in an “overcut” sidewall profile (a sidewall angle less than 90 °), while for a negative photoresist, such an

exposure profile versus depth results in an “undercut” sidewall profile (a sidewall angle greater than 90 °).

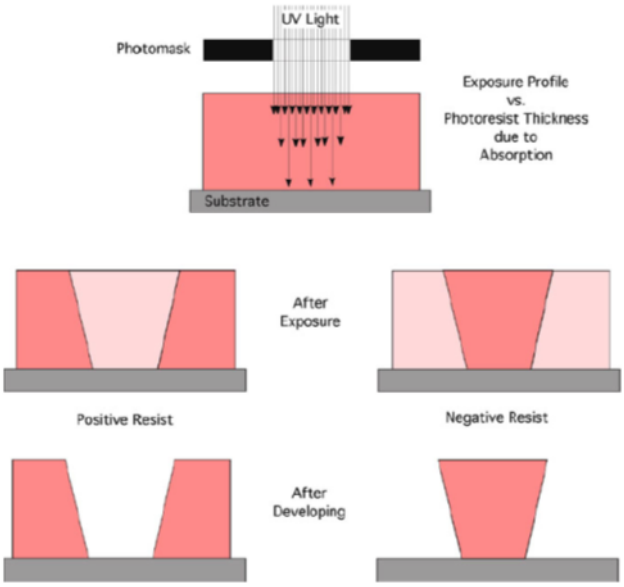

Figure 18 – Edge profile of photoresist layer resulting from absorption of light during exposure [36]

Modern demands on microfabrication lithography processing are increasing, thus pushing the technology forward smaller structures of higher aspect ratio. In order to meet increasing needs greater attention must be paid to each component and step of microfabrication to ensure top performance of the manufactured components. The most important component in pattern forming is photoresin/photoresist polymer, which is used to create an intended design. Properties of the pattern directly depend on photoresist performance during and after exposure, such as mechanical stability, homogeneity and uniformity of the pattern (height and periodicity). Different characterization methods are used to estimate photoresist behavior and optimize processing parameters such as exposure energy and development time according to the acquired information. One of the standard methods to evaluate sensitivity and contrast of the photoresist in use as well as optimal exposure energy is contrast (sensitivity) curve (figure 19).

The contrast curve plotting and contrast evaluation was carried out as noted in [13] and based on the assumption that the photoresist response is a function only of the exposed energy [15]:

$$\gamma = \left(\lg \frac{D_2}{D_1} \right)^{-1}, \tag{3}$$

where D_1 – exposure energy for 10 % photoresist remaining, mJ/cm^2;

D_2 – exposure energy for 90 % photoresist remaining, mJ/cm^2.

For precise parameter estimation generalized logistic function was used [13] to fit experimental data

$$Y(t) = A + \frac{K-A}{\left(1+Qe^{-B(t-M)}\right)^{\frac{1}{\nu}}}. \quad (4)$$

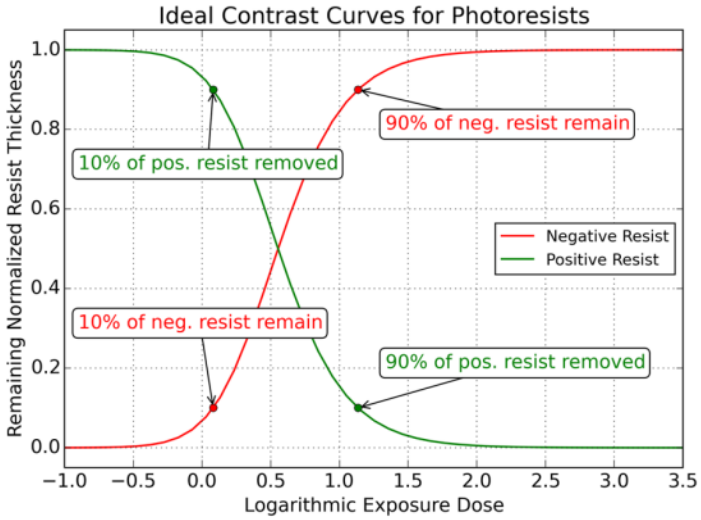

Figure 19 – Ideal contrast curves for positive (green) negative (red) photoresist to define sensitivity and optimal exposure energy (dose) for photoresist

The contrast curve allows determining several important parameters for photoresist processing: photoresist sensitivity and optimal exposure energy value. Sensitivity is characterized by the slope of the curve and the optimal exposure energy can be estimated from the complete crosslink plateau. As in case of UV lithography exposure is characterized not by dose, but by surface exposure energy, it is important to take into account absorption loss in intensity during penetration of radiation into photoresist layer. Thus, for different thicknesses different values of exposure energy will ensure complete cross-link.

To obtain contrast curve an intended set of samples is required. The processing of samples is similar to standard UV LIGA process, excluding electroplating part and adding height measurement after resist development. The scheme of the process is shown in figure 20. First step is a wafer surface pretreat by spraying hexamethyldisilazane (HDMS) with simultaneous heating. Following step is photoresist spin-coating with a consequent soft bake at hot plate. Note that for better understanding of resist sensitivity for UV lithography it is necessary to study several thicknesses. Thereafter soft bake the uniformity and homogeneity of spin-coated resist should be controlled by thickness measurements in different point of the wafer.

Exposure with UV light should be carried out after soft bake, although sometimes relaxation period for the wafers is required to ensure drying of the resist. To ensure precise dose value and uniformity of intensity distribution within exposure region preliminary

measurement of intensity values in different points should be performed. Exposure for contrast curve is performed using a double mask: first mask is a mask with test structures of different size and the second is an opaque mask with a slit to split in order to provide with several regions exposed with different exposure energy threshold. Exposure energy is usually varied by increasing/decreasing exposure time as the UV source has known intensity. After exposing a single region using test mask and slit mask, the latter is rotated to exposure next sector of the wafer with increased energy value. Energy region should be estimated in order to obtain underexposure with no sufficient cross-link for structure to remain on the wafer for the first sectors and to reach complete cross-link plateau for the last regions. It is desired to capture transition region and obtain the maximum possible amount of points for this part of the contrast curve (maximum amount of different remaining thicknesses values). After post exposure bake (PEB) and consecutive development the final measurements of remaining thickness should be performed with profilometer device or other techniques available.

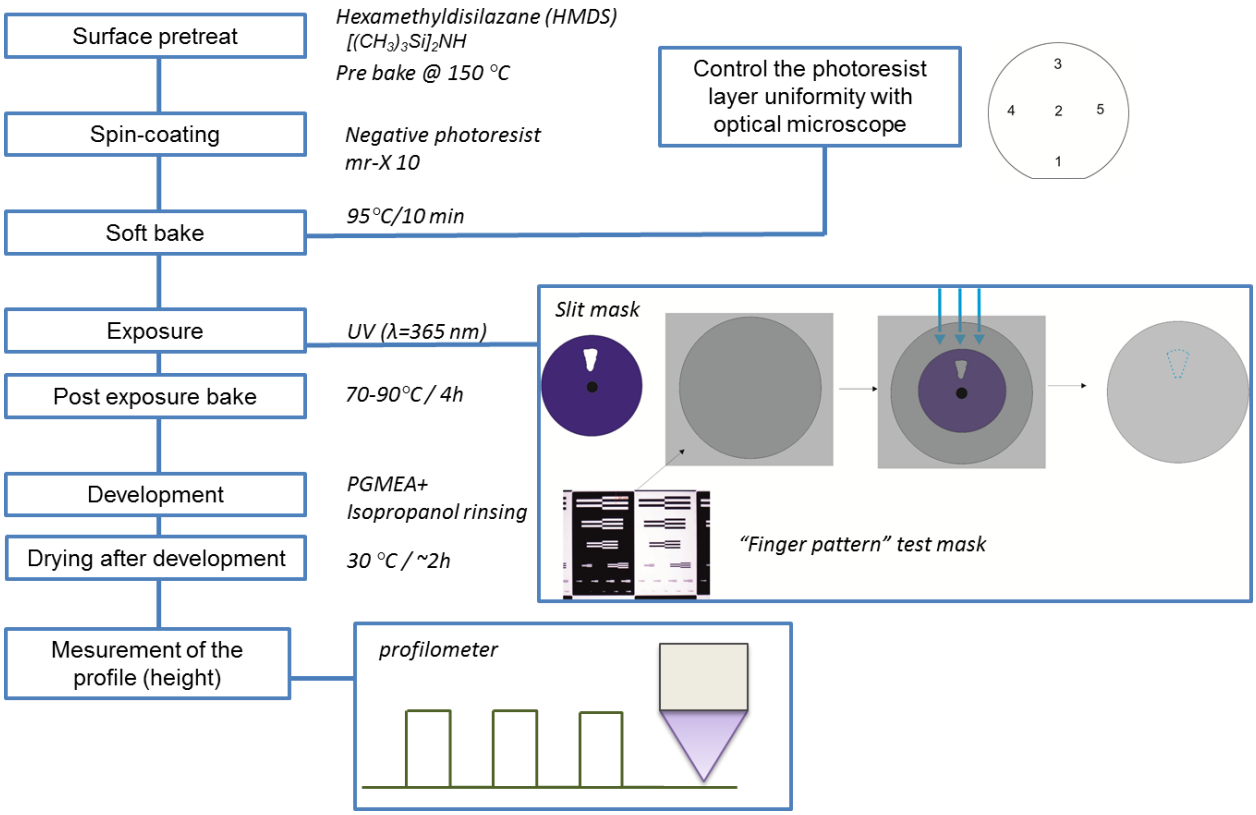

Figure 20 – Scheme of processing sequence to obtain contrast curve

Chapter 3 Results and discussion

3.1 Sensitivity Curve for negative epoxy-based photoresist

A set of samples was prepared to carry out contrast curve procedure. Silicon wafers with the thickness of 500 μm were sputtered with a thin (few nm) layer of HDMS during substrate pretreat with heating up to 150 °C for 30 minutes to increase the adhesion of the photoresist to the wafer. Using different regimes to achieve different layer thickness the epoxy-based negative mr-X 10 photoresist (MicroChem) was spin-coated on the wafers. The photoresist consists of a photoacid generator and acid-labile groups. Spin-coating parameters are listed in the table 1.

Table 1 – Spin-coating parameters for Contrast Curve samples (mr-X 10 photoresist)

Resist layer thickness	Spin Coating parameters (time // spin speed // acceleration)
5 μm	60 sec // 5000 rpm // 1500 rpm/sec.
10 μm	60 sec // 2000 rpm // 1500 rpm/sec.
15 μm	1) 30 sec // 500 rpm // 500 rpm/sec; 2) 60 sec // 0 rpm // 1500 rpm/sec; 3) 60 sec // 1200 rpm // 1500 rpm/sec.
20 μm	1) 30 sec // 500 rpm // 500 rpm/sec; 2) 60 sec // 0rpm // 1500 rpm/sec; 3) 60 sec // 850 rpm // 1500 rpm/sec.

The soft bake was performed using hot plates at temperature of 95 ºC for 10 minutes. Exposure was carried out with mercury UV lamp LH5. The stability and distribution of the total incident radiation power was controlled by Karl Suss UV intensity meter model 1000. The intensity value was 15 mW/cm^2 with 1 mW/cm^2 deviation from the center to the edge of FoV, the measurements were performed for i-line of the mercury spectrum (λ = 365 nm). The exposure was done using a double mask geometry described in *Chapter 2 Section 2.2*. The lower mask was a Cr-Quartz mask with alternating dark and light tone regions with pattern of structure sizes from 2 up to 60 μm. The wafer area was divided into 15 sectors exposed with different surface energy value using a constant energy step, thus the surface energy was tuned within a determined range by changing the exposure time. Exposure was carried out using hard contact alignment: the wafer and the mask were placed in the vacuum chamber to ensure elimination of diffraction effects.

The exposed samples were subjected to post exposure bake in the oven for 4 hours with temperature changing from 70 up to 90 ºC. A wet development of the exposed resist layers was carried out in three steps: first for 10 minutes in propylene glycol

monomethyl ether acetate (PGMEA) in order to dissolve unexposed area of mr-X 10 photoresist layer, then in the fresh PGMEA for the same time and the samples were rinsed in the isopropanol alcohol. After development, the samples were air dried in an oven at 30 ºC. For all development-rinsing-drying steps the samples were placed on a special holder with the resist layer upside down to prevent structure damage due to the contact with equipment in use. After drying, the height of the formed micropattern was measured with a long scan profiler Tencor P-2 with an accuracy of 25 Å.

The results of the contrast curve measurements for the first measured contrast curve are shown in figure 21 *d.* Valuable information which can be obtained from the contrast or sensitivity curves, for a given patterning resist material, is the optimal surface exposure energy. Here by optimal exposure energy we mean the value of surface energy, which is sufficient to obtain a full cross-link of the photoresist and defect-free pattern. Optimal dose values were estimated from the contrast curve samples, taking into account the remained thickness as well as the pattern quality evaluated with optical microscope (figure 21 *a-c*).

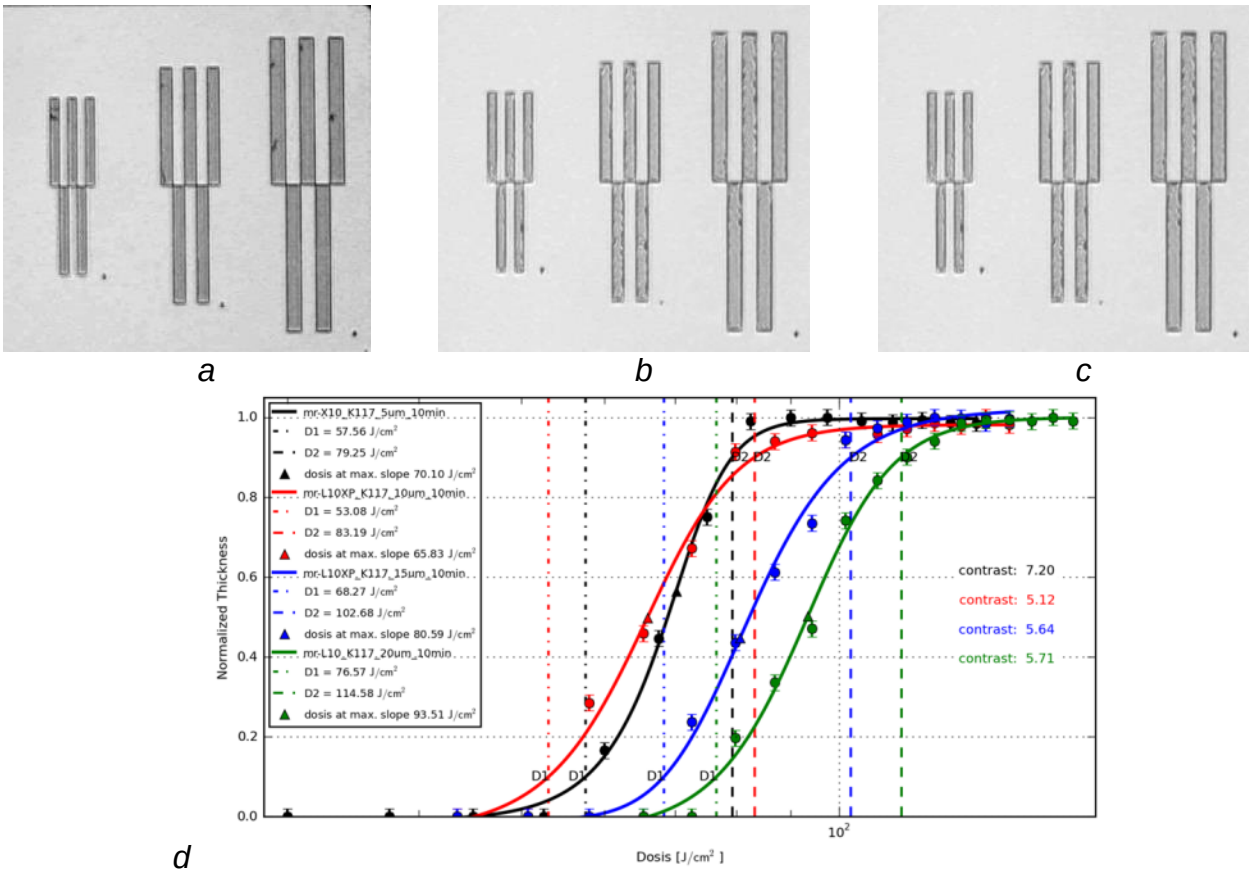

Figure 21 – Patterns obtained for optimal exposure energy section with contrast curve samples for mr-X 10 thickness *a)* 5 µm (~110 mJ/cm^2), *b)* 10 µm (~130 mJ/cm^2), *c)* 20 µm (~180 mJ/cm^2); *d)* contrast curve for mr-X 10 for four thicknesses: 5 µm (black), 10 µm (red), 15 µm (blue), 20 µm (green). Development time for all wafers was 10 minutes

After characterization of the curve behavior it was noted that the contrast for samples with photoresist thicknesses higher than 5 μm is significantly lower, although only shift in the position of the curves was expected due to UV light absorption of the layer. It was suggested that the development time was not adjusted for thicker layers of photoresist and thin residual layer of unexposed resist remained on the surface for the samples with resist thicknesses 10 μm, 15 μm and 20 μm. As a profilometer measures the relative height as a distance from the lowest point of the pattern profile to the highest, the remaining layer provoked acquisition of false values for cross-linked resist height.

To check the theory it was decided to perform a second measurement where longer development times were employed in order to achieve complete dissolution of unexposed photoresist. The first test approach was to estimate the adjusted development time with modification derived from the ratio between the start surface exposure energies, considering that development time for 5μm photoresist thickness is optimal (10 minutes). By optimal development time here we mean a period of time sufficient to completely dissolve the unexposed photoresist areas in PGMEA. Therefore, according to the suggested theory, adjusted development time for a resist layer of a certain thickness can be estimated as

$$t^{D}_{thickn.} = t^{D}_{5\mu m} \cdot \frac{E^{start}_{thickn.}}{E^{start}_{5\mu m}}, \quad (5)$$

where $t^{D}_{5\mu m}$ – development time for 5 μm resist thickness (10 minutes);

E_{thickn}^{start} – start surface exposure energy, mJ/cm^2;

$E_{5\mu m}^{start}$ - start surface exposure energy for 5 μm resist thickness, mJ/cm^2.

Adjusted development times for Contrast Curve samples are listed in Table 2.

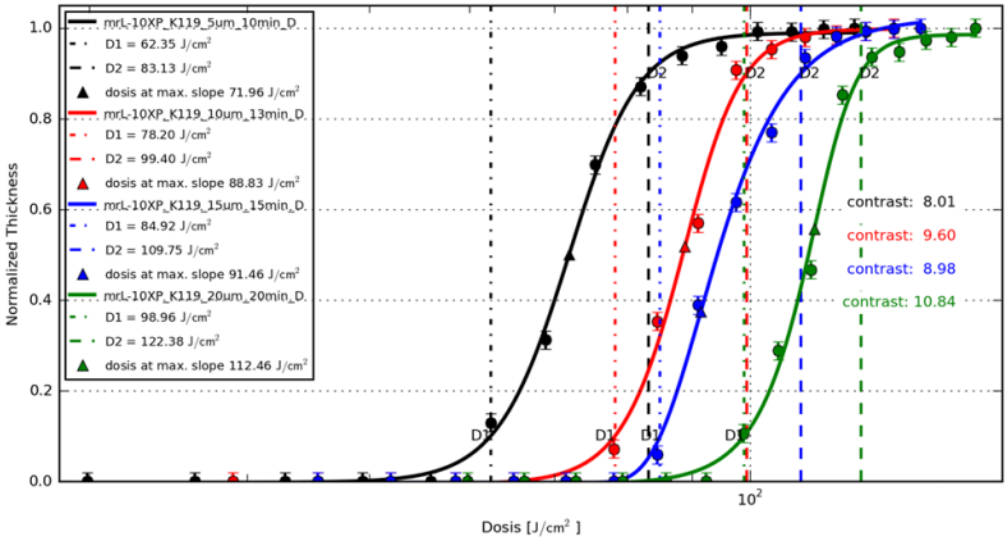

Figure 22 – Contrast curve for mr-X 10 for four thicknesses: 5 μm (black), 10 μm (red), 15 μm (blue), 20 μm (green). The development time was adjusted according to equation 5 for photoresist layers thicker than 5 μm

Contrast curves obtained for samples with adjusted development time are plotted in figure 22. As one can see the contrast has significantly increased in comparison with first measurements. One can notice that the contrast curves are shifted forward to higher surface energies, because the exposure energy is not a volumetric characteristic, thus contrast curves are dependent on the resist thickness. Actually the contrast value itself would be thickness-dependent, as for a negative photoresist profile the “undercut” is typical, meaning that more material will be dissolved away at the bottom. If the difference between the top and the bottom energy is quite big, which is the case for higher structures, the bottom energy will not provide sufficient cross-link for structures to stay attached to the wafer, and thus they will be washed away during the development and rinsing. As an increased stress is applied to the bottom while its mechanical stability provided by cross-linking is decreased the structures will be either washed away or completely cross-linked, meaning the height close to the initial photoresist thickness. This will result in an increased contrast as the contrast curve will be approaching a step function shape. Thus, for thicker negative photoresist layers the contrast value obtained with UV lithography should be higher, than for thinner ones. Although as it can be noted in the figure 22, the 15 µm contrast curve is out of this dependency, which might indicate that further optimization of the development time is required. As the dissolution time should depend not only on the energy of exposure, but also on the area of the photoresist, meaning photoresist thickness in our case as the mask pattern in use was the same. The impact of absorption of the layer should also be taken into account, as it is not the exposure dose incident on the resist which causes a change in the development rate, but the dose which actually makes it into the resist that matters [37].

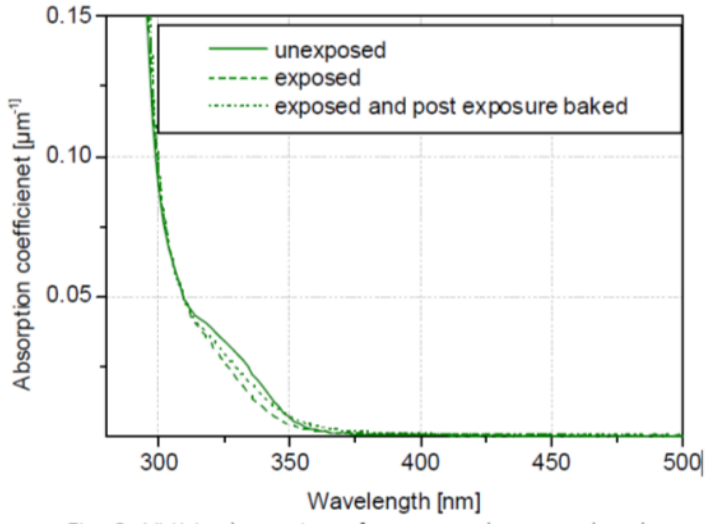

Figure 23 – UV/vis absorption of unexposed, exposed and post exposure baked mr-X [38]

As it was noted, the optimal energies estimated from the contrast curves and images of micropatterns are the values of surface (top) energies, while bottom energies should be calculated taking into account that part of the UV light intensity was absorbed by the photoresist layer. To estimate the bottom exposure energy values absorption coefficient information was used reported in [38]. From the figure 23, absorption coefficient for mr-X series negative photoresist is 0.005 μm^{-1}. If the surface intensity of the UV radiation is J_0 and the intensity on the bottom is J, then bottom exposure energy can be derived as

$$E_{bottom} = J \cdot t = \left(J_0 - \Delta J\right) \cdot t = J_0 \cdot t \cdot \left(1 - L \cdot \mu\right), \quad (6)$$

where ΔJ – intensity loss due to absorption;

t – exposure time, seconds;

L – photoresist thickness, μm;

μ - absorption coefficient of mr-X photoresist, μm^{-1}.

The bottom exposure energy here is calculated taking into account only the absorption phenomena, while for thicker layers the scattering phenomena arise decreasing UV intensity in a certain point on the wafer surface, but we consider these effects negligible as relatively small thicknesses were studied using vacuum contact alignment.

Therefore, the adjusted development time can be as well estimated as

$$t_L^D = t_{5\mu m}^D \cdot \frac{L / 5\mu m}{E_L^{opt.bottom} / E_{5\mu m}^{opt.bottom}}, \quad (7)$$

where $E_L^{opt.bottom}$ – optimal bottom exposure energy for a layer of thickness L, mJ/cm^2;

$E_{5\mu m}^{opt.bottom}$ - optimal bottom exposure energy for 5 μm resist thickness, mJ/cm^2.

The equation 7 provides with longer development times for intermediate photoresist thicknesses of 10 μm and 15 μm. All processing parameters obtained for the contrast curve are listed in the table 2.

Table 2 – Exposure (optimal surface and bottom energies) and calculated development parameters for contrast curve samples

Resist layer thickness, μm	Optimal surface exposure energy, mJ/cm^2	Bottom exposure energy at optimal surface energy, mJ/cm^2	Adjusted development time (Eq. 4), min	Adjusted development time (Eq. 6), min
5	110	107	10	10
10	120	114	13	19
15	150	140	15	23
20	180	162	23	26

3.2 Two-dimensional gratings patterning with UV LIGA

3.2.1 Substrate preparation and photoresist spin-coating

UV LIGA for manufacturing of 2D gratings was carried out using the process chain similar to the contrast curve samples preparation, but with several application-related changes. The main overview of the process is shown in the figure 24.

Low-absorbing substrate wafers were used for grating fabrication in order to ensure the maximum transmission of the radiation, i.e. to achieve the maximum wavefront modulation. In our case the substrates were 200 μm Silicon wafers with few nanometers of Ti and TiO_x to create a conductive contact layer for the concluding electroplating. There were two sample sets: first consisted of 6 wafers and the second of 2 wafers.

In order to prevent a presence of particles and inclusions in the photoresist and to improve its adhesion to the wafer, intended substrate preparation should be performed to guarantee that it is free of impurities and moisture. Oxygen plasma cleaning was employed with subsequent baking at 120 ºC and cooling down to room temperature immediately before coating.

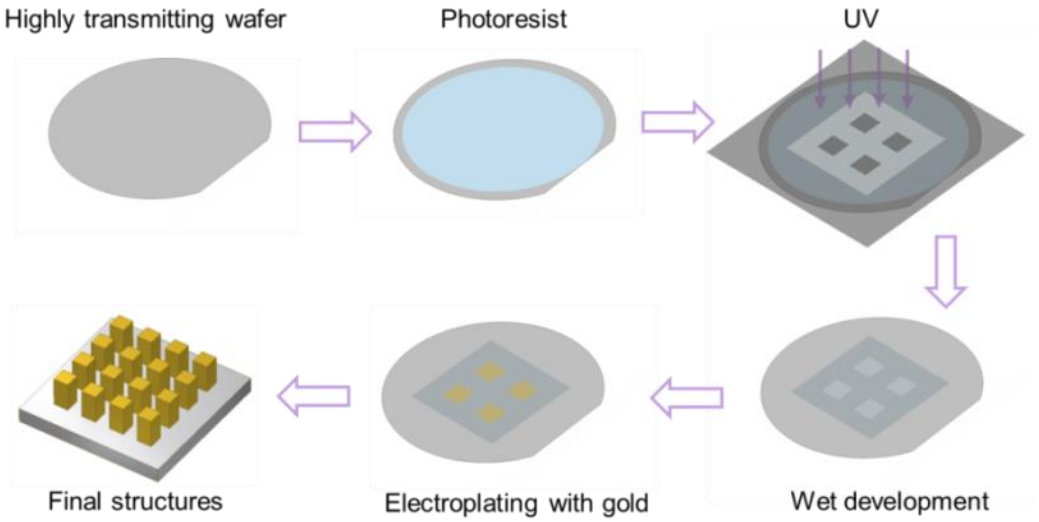

Figure 24 – Fabrication process steps of UV LIGA

Spin-coating of TI PRIME adhesion promoter was performed according to the recommendations from technical data sheet [38]. TI PRIME forms a physically bonded sub-monolayer of the active compound after solvent evaporation. Subsequent baking step of the primed substrate at 120 °C chemically activated the adhesion promoter thus forming the desired hydrophobic surface allowing subsequent resist coating with improved wetting and adhesion between TiO_x and photoresist. Immediately after the primed substrate baking spin-coating of negative mr-X 10 photoresist was performed to achieve 10 μm, 20 μm, 30 μm and 40 μm thicknesses using the parameters listed in the table 3. A soft bake

to remove the solvent content from the sample was carried out at 95 °C on the hot plates for time periods from 10 to 20 minutes depending on the photoresist layer thickness.

Table 3 – Spin-coating parameters for 2D gratings (mr-X 10 photoresist)

Photoresist layer thickness	Spin Coating parameters (time // spin speed // acceleration)
10 μm	60 sec // 2000 rpm // 1500 rpm/sec.
20 μm	1) 30 sec // 500 rpm // 500 rpm/sec; 2) 60 sec // 0rpm // 1500 rpm/sec; 3) 60 sec // 850 rpm // 1500 rpm/sec.
30 μm	1) 30 sec // 500 rpm // 500 rpm/sec; 2) 60 sec // 0 rpm // 1500 rpm/sec; 60 sec // 500 rpm // 1500 rpm/sec.
40 μm	30 sec // 700 rpm // 1300 rpm/sec.

3.2.2 Photoresist pattern formation

The exposure of photoresist layers was performed using EVG mask aligner with 2.85 mW/cm^2 radiation intensity (0.15 mW/cm^2 deviation) using the filter for wavelengths shorter than 365 nm. The photomask for exposure (figure 25) was a 5 inch Cr-Quartz mask purchased from Compugraphics (Jena, Germany). It was covered with thin layer of Teflon in order to protect the mask. The exposure was carried out with soft contact mode (no vacuum) in order to reduce diffraction effects but also to prevent sticking the photoresist layer to the mask. Theoretically optimal exposure energy depends on photoresist thickness, solvent, UV sensitivity, absorption on the exposure spectrum, power and coherence of UV lamp, but it can be empirically estimated using the contrast curve method. The exposure surface energies were estimated by comparison of the data obtained for contrast curve samples (*Section 3.1.* of this Chapter) exposed with higher intensity (LH5 lamp) and laboratory investigations results from other students (EVG mask aligner).

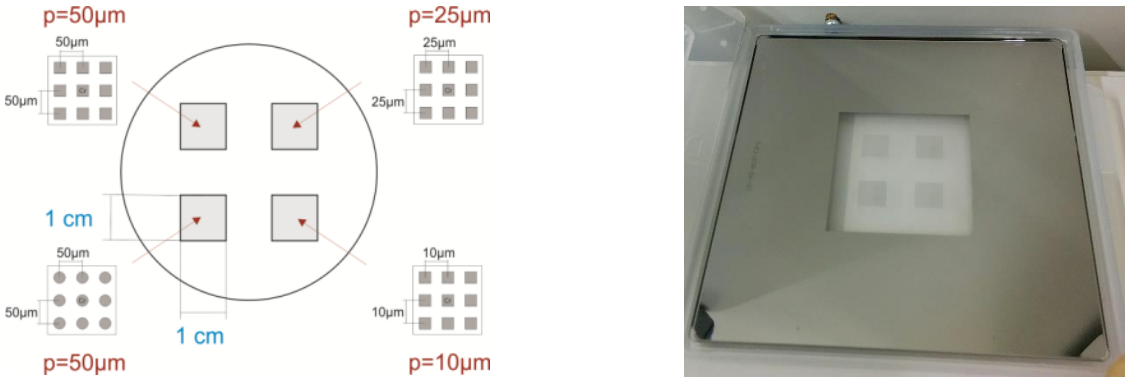

a *b*

Figure 25 – Cr-Quartz mask used for exposure with UV lamp: *a*) schematic layout, *b*) picture of the mask

The exposed samples were subjected to PEB in the oven for 4 hours within temperature range from 70 up to 90 ºC. Wet chemical development of the exposed resist layers was carried out in three steps: first in recycled propylene glycol monomethyl ether acetate (PGMEA) in order to dissolve unexposed area of mr-X 10 photoresist layer, then in the fresh PGMEA for the same time and then the samples were rinsed in the isopropanol alcohol. Development times were adjusted according to *Section 3.1.* During the development, the photoresist pattern was formed due to etching of unexposed regions. After development samples were air-dried in the convection oven at 30 ºC. The optical microscope image of the pattern obtained with the steps described above is shown in the figure 26. Sharp definition of the structures and high degree of periodicity was observed for all periods for photoresist thickness up to 25 μm (figure 26 *a*). Although, for photoresist thickness of 30 μm and thicker structures with period of 10 μm undergo undesirable crosslink caused by diffraction limit of photolithography (figure 26 *b*).

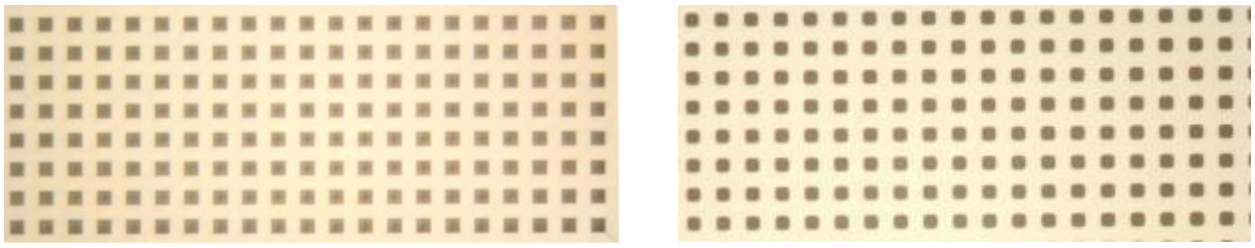

a *b*

Figure 26 – Optical microscope images of the photoresist pattern observed after development: *a*) grating period 25 μm, photoresist thickness 25 μm; *b*) grating period 10μm, photoresist thickness 30 μm

Thorough optical microscope examination of photoresist pattern of 10 μm period was conducted to evaluate uniformity of the diffraction effects. The grating area was divided into 9 region imaged separately (figure 27). It was noticed that the degree of undesired cross-linked varied dramatically for those regions: the regions 1, 4 and 7, which were closer to the center of the wafer and consequently closer to the center of intensity distribution, underwent more active cross-linking reaction affecting the areas covered by opaque Cr regions during exposure. The same behavior was shown by the other wafer from the same sample set and processed with exactly the same parameters. This implies that cross-linking process strongly depends not only on the exposure energy, but also on the intensity of the radiation.

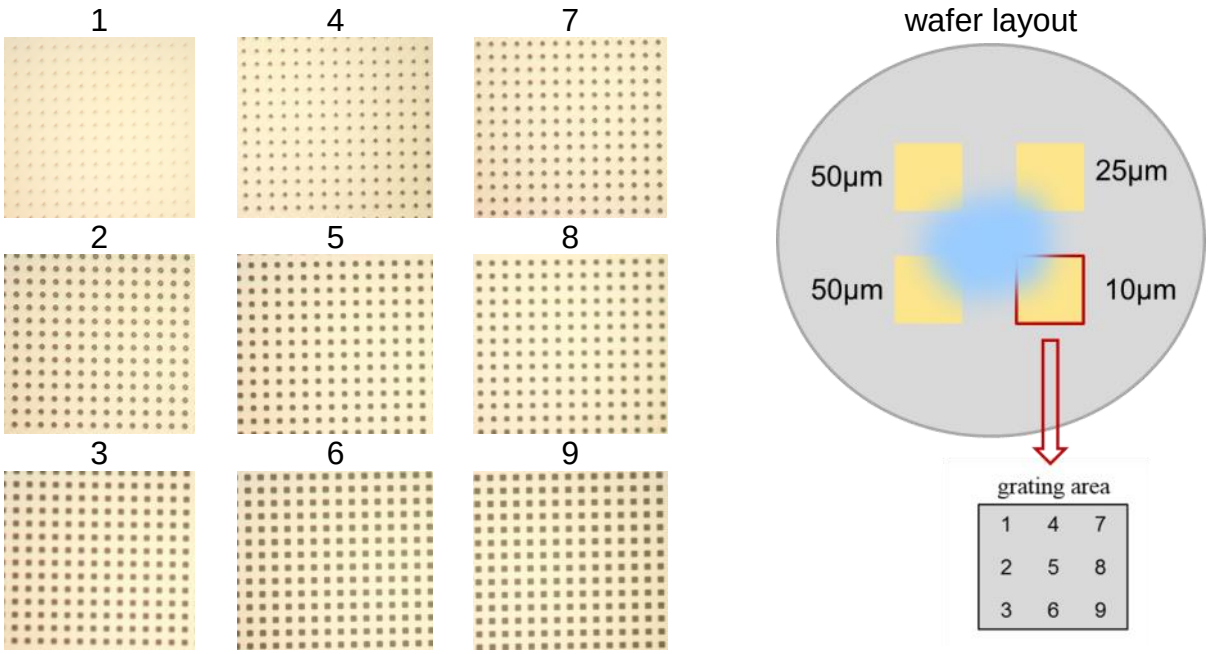

Figure 27 – Optical microscope images (1-9) of respective regions of the grating area. Considering the wafer layout one can notice, that regions 1, 4 and 7 were the closest to the center of the wafer

3.2.3 Gold electroforming

Reactive ion etching (RIE) is an optional step applied in case of fabrication of high aspect ratio structures and aimed to clear the resist pattern in the bottom part of the grating. It is of great importance for grating fabrication to insure that there is no residual photoresist layer left and there is an access to the conductive wafer surface to be electroplated with gold or other desired metal. In case of the structures manufactured in this thesis the first attempt was to ignore this step as the aspect ratio did not exceed 3. Although due to the complexity of the grating pattern results of first electroplating have shown a lot of cells which were plated with gold partially or were not plated at all. Based on the experience, the other sample from the set with the same parameters was subjected to RIE prior to the electroplating step. Etching was performed with oxygen plasma for 5 minutes at 120W/10mTor. The improvement of gold pattern is shown in figure 28.

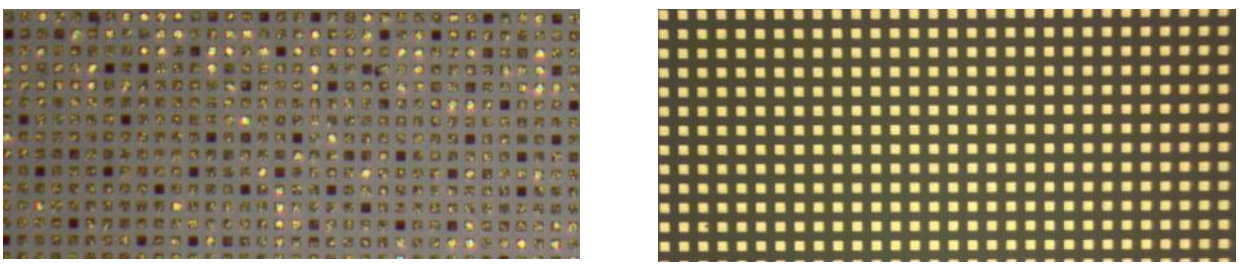

a *b*

Figure 28 – Optical microscope images of electroplated gratings without (*a*) and with (*b*) prior RIE procedure

Electroplating current, voltage and duration time are defined by the amount of gold that should be plated on the wafer. This value is determined by the height of designed structures, which is usually 75-80% of photoresist layer thickness, and the area that should be electroplating. The electroplating area for the purchased mask was calculated manually based on the layout. The values for each region as well as total electroplating area are listed in the table 4. Considering the mask layout (figure 25), edge framing with polymethylmethacrylate (PMMA) to prevent electroplating of the wafer edges, where there was no photoresist coverage.

Table 4 – Electroplating area of the purchased mask

Region name	Hole shape	Period, μm	Electroplating area, mm^2
Region 1	square	50	25.000
Region 2	square	25	25.000
Region 3	square	10	25.000
Region 4	round	50	19.635
		Total area	94.635

Gold electroforming was performed in the electroplating bath at the temperature of 55 ºC. Current and start voltage were adjusted depending on electroplating area and intended gold height. After electroplating for the gratings with 40 μm photoresist layer thickness consequent photoresist stripping with oxygen plasma was performed. Scanning electron microscopy (SEM) images of the gratings with stripped (figure 29 *a*) and unstripped (figure. 29 *b*) photoresist are showing the final views of manufactured gratings of 50 μm period.

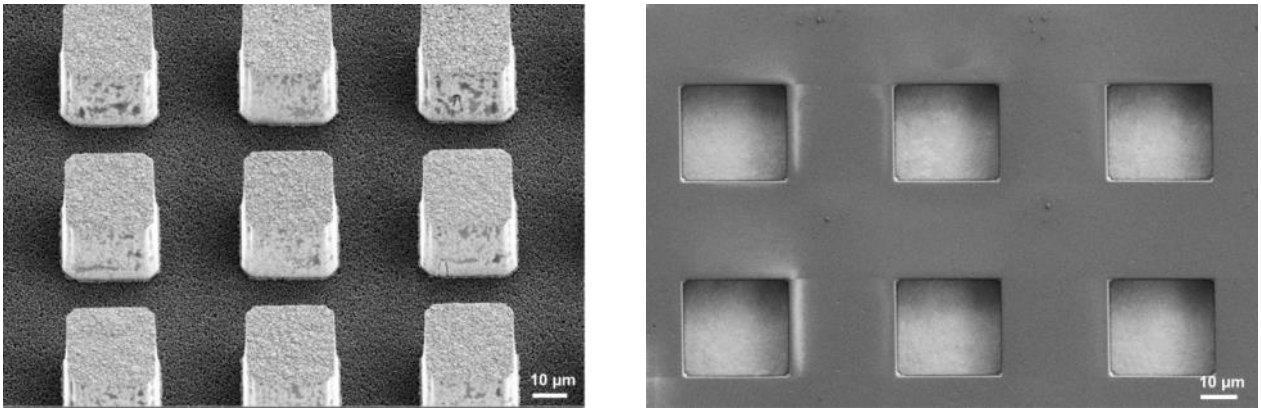

a *B*

Figure 29 – SEM images of the gratings with stripped (*a*) and unstripped (*b)* photoresist for 50 μm period structures

3.3 Gratings quality evaluation

3.3.1 Scanning electron microscopy

Grating quality evaluation was first performed with optical and scanning electron microscopes to estimate uniformity of the grating pattern, sharpness of structures edges, sidewalls geometry and to characterize it quantitatively by measuring period of the grating and height of the gold structures. For the gratings with gold height from 5 to 15 μm structures with period down to 10 μm is available, although the shape of the structures is affected by diffraction in the corners of the square pillars. For gold structures higher than 20 μm electroplating of region with period 10 μm was not possible due to excessive cross-linking of the photoresist and significant distortion of the initial pattern. Overall grating parameters with a brief comment on their quality are listed in the Table 5.

Table 5 – Characteristics of two-dimensional gratings of different thickness and period

Wafer number	Average photoresist height, μm	Average gold height, μm	Available periods, μm	Quality and comments
1458-2	9	5	none	Low
1457-2			10, 25, 50	Excellent for 25 and 50 μm; 10 μm is plated, but the shape is distorted by diffraction effects.
1459-2	20	14	10, 25, 50	Structures are very well defined and sharp edges for 25 and 50 μm, 10 μm is plated, but partially detached and over cross-linked.
1460-2		15	10, 25, 50	Good quality, nevertheless worse than 1259-2 for 25 and 50 μm; gold agglomerates above the structures; 10 μm is plated but over cross-linked
1461-2	32	30*	25, 50	Over-plated but uniform 25 and 50 μm; 10 μm is not plated.
1462-2		24		Slightly influenced by diffraction by sufficiently sharp edges for 25 and 50 μm; 10 μm is not plated
1488-2	40	28	25, 50	Slight changes of duty cycle for 50 μm, stronger for 25 μm; corners of square structures are affected by diffraction: deviation of period ±0.1 μm; deviation of size from bottom to top ±1.0 μm (for square p = 50 μm), ±1.25 (for square p = 25 μm), ±0.8 μm (for round p = 50 μm).
1489-2				

In the figure 30 SEM images of the 50 μm period square gratings on the wafers number 1459-2 (*a*) and 1460-2 (*b*) are shown. These samples were processed with the same parameters and at the same time in order to have a reference between them and

also to have a substitution in case of wafer damage. Although processing of the wafers was performed exactly the same, photoresist performance was slightly different. One can notice that the sample 1459-2 showed much higher quality; the structures are very well-defined, the edges are smooth and there is only a minor diffraction effect observed in the corners of the square cell finned with gold. Although the sample 1460-2 exhibits wave-like shape of the photoresist mesh border (figure 31 *a*-*b*). The photoresist formation in the border looks like it was caused by interference occurred during exposure, which means that the source has a partially coherent radiation. The influence of these effects is increasing for smaller structures and thicker photoresist layers (figure 32 *a*-*b*). It causes a significant shape distortion, and for 32 μm photoresist layer thickness it led to the situation when electroplating for those structures was not possible (figure. 32 *b*).

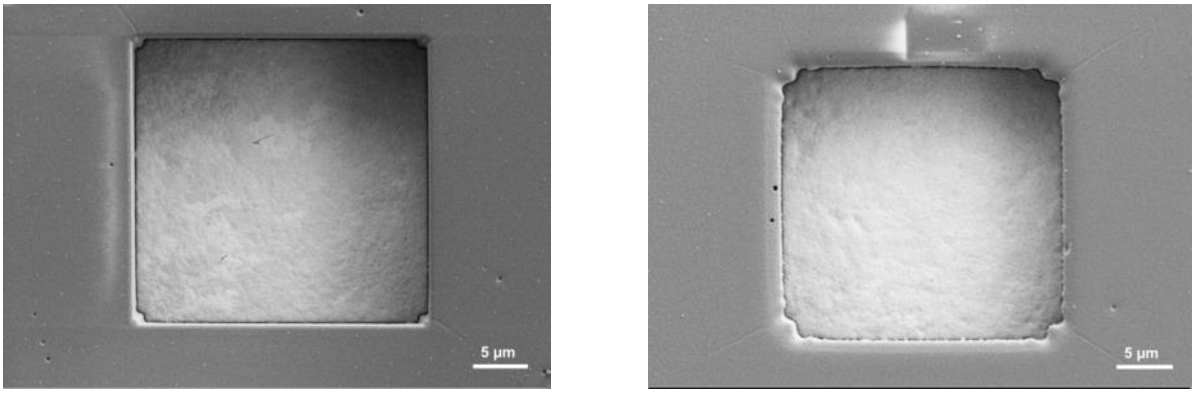

a *b*

Figure 30 – SEM images of a single gold structure of 50 μm period for square gratings on the wafers *a)* 1459-2 and *b)* 1460-2 respectively processed with the same parameters

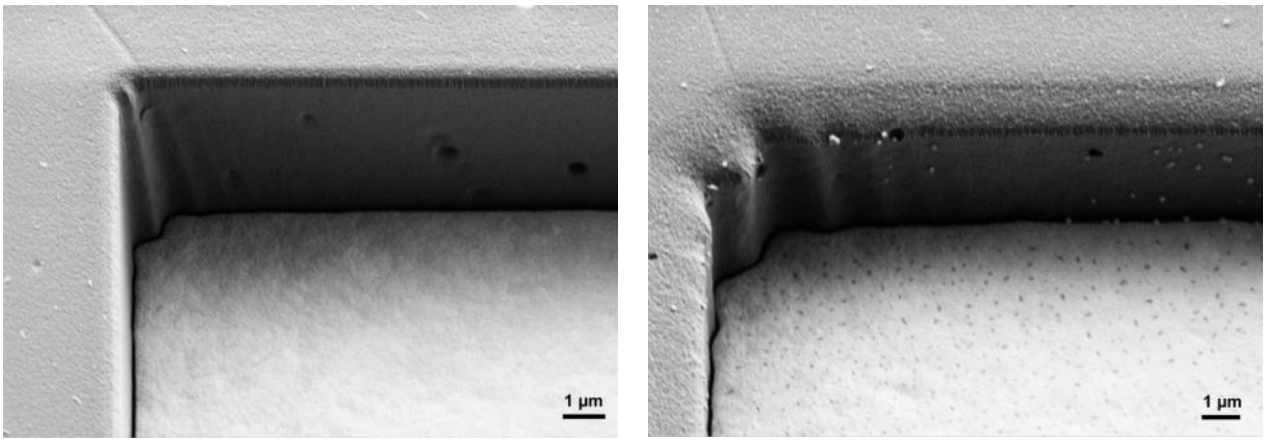

a *b*

Figure 31 – SEM images of the corner of the photoresist mesh of 50 μm period for square gratings on the wafers *a)* 1459-2 and *b)* 1460-2 respectively processed with the same parameters

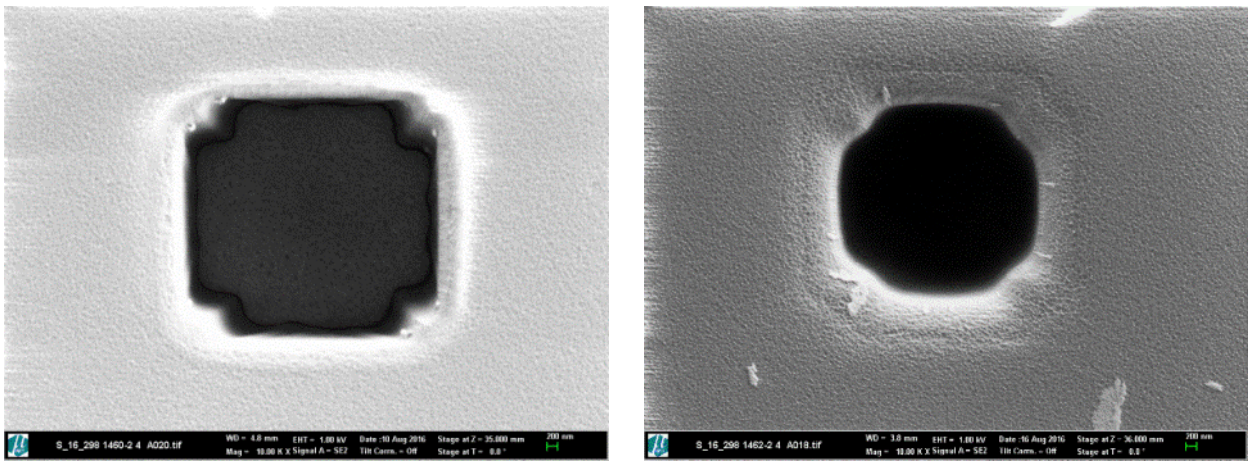

a *B*

Figure 32 – SEM images illustrating shape distortion due to diffraction effects in photoresist layer of *a)* 20 μm (wafer 1460-2) and *b)* 32 μm (wafer 1462-2) thickness

Another example of the grating of 25 μm period and 28 μm gold height with stripped photoresist is shown in the figure 33. One can see that grating pattern is clear and uniform, no structures are collapsed or detached (figure 33 *a*). Each pillar of the grating is wider in the bottom and smaller on the top, which is due to utilization of a negative photoresist in the photolithography process. This means that period of the grating on top and in the bottom is slightly different from intended (average period is P = 25.1 ± 0.2 μm). Although the duty cycle of the pattern was affected strongly than the period. Analysis of SEM images has shown that for the top of the grating duty cycle is 0.472 and for the bottom 0.576. Thus the period variation is less than 1 % and the average duty cycle is DC = 0.0524 ± 0.052. It is important to note, that analyzed grating is with the highest aspect ratio among fabricated gratings with sufficient quality, which mean these distortions are much less for other gratings. From the application side such a distorted shape of the structures might slightly decrease the efficiency of wavefront modulation, but on the other hand it provides structures with additional mechanical stability.

As it was mentioned before, different shapes of the structures were tested to compare their final quality. The two-dimensional X-ray gratings of the 50 μm period and 28 μm gold heights are presented in the figure 34. As one can see in the figure 34 *a-b* grating patterns of both shapes are clear and uniform, structures are well-defined and exhibit high degree of periodicity. Single pillars of square and round shape shown in the figure 34 *c-d* both obtain wider foundation and narrower top, but here the deviation is smaller than shown in the figure 33 *b*. For square pillar top duty cycle is 0.494 and the bottom – 0.534, which means that the average DC = 0.5140 ± 0.020. For the round pillar top duty cycle is 0.498 and for the bottom – 0.530, which means that the average DC = 0.5140 ± 0.016. No period variation within accuracy of the measurement was detected. This means that the variation of the top and bottom sizes of the pillars is different for

square and round shapes, but average duty cycle is the same. Although for the structures of smaller period one can profit from decreased influence of diffraction in patterning of round structures instead of square ones.

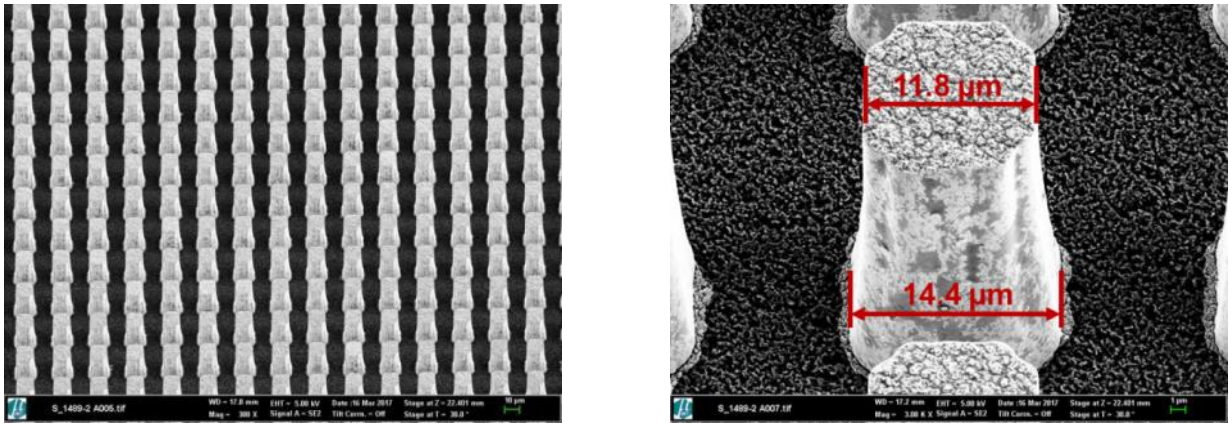

a *B*

Figure 33 – SEM images of two-dimensional X-ray grating of 25 µm period and 28 µm gold height: *a)* overview of the pattern, *b)* single structure

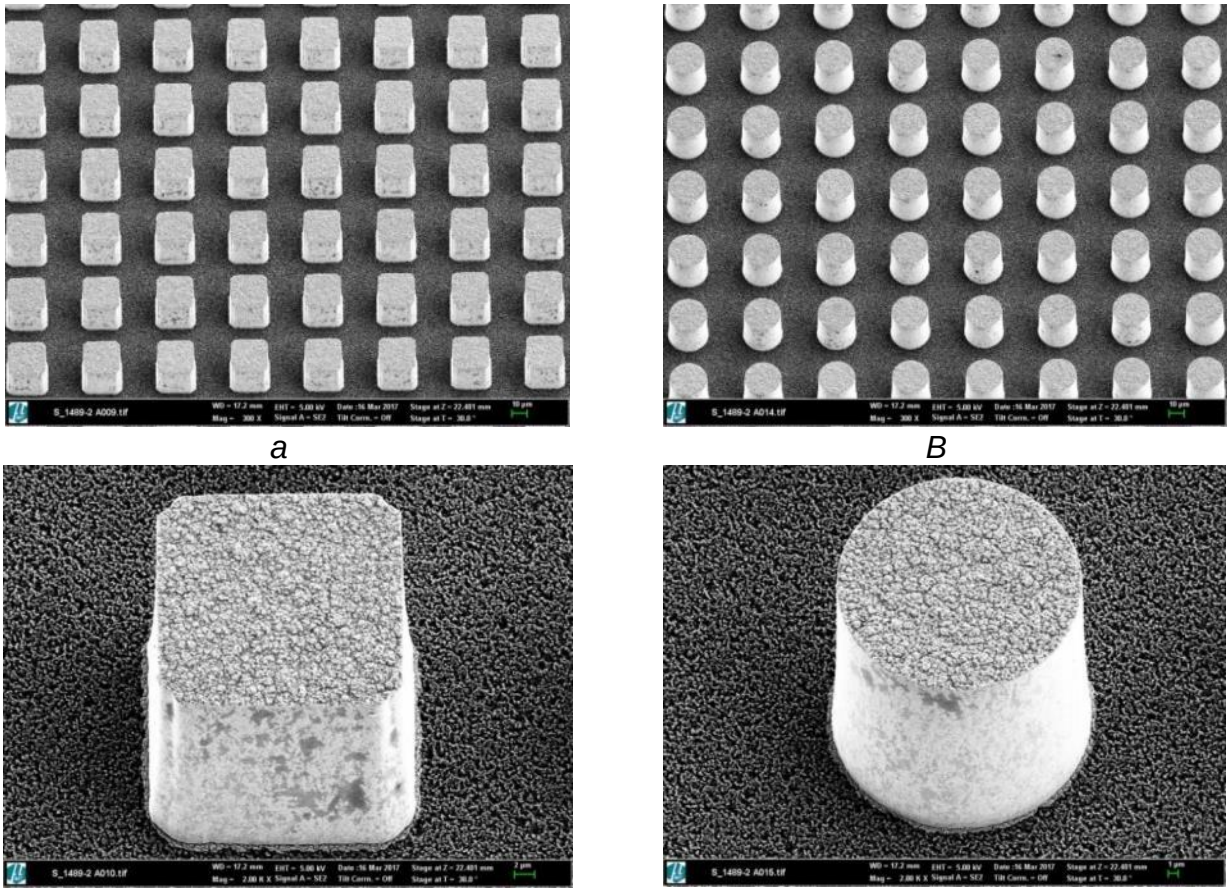

a *B*

c *D*

Figure 34 – SEM images of two-dimensional X-ray gratings of the 50 µm period and 28 µm gold height: *a)* and *b)* are overviews of the square and round shapes respectively, *c)* and *d)* are single square and round pillars

3.3.2 Grating quality evaluation algorithm

To test the gratings and establish an algorithm to estimate their quality and performance, radiography measurements were conducted using the TopoTomo beamline at the ANKA synchrotron radiation facility of the KIT. The main idea of the Grating quality evaluation algorithm for testing it within radiography setup is in comparing intensity distribution obtained on the detector plane with simulated intensity map from ideal grating. By transforming simulated ideal grating one can estimate quantitatively the wavefront modulation and characterize structural changes in the real grating. Ideal grating is represented by two-dimensional array with dimensions based on the digital image obtained from the real data (figure 35 *a*-*c*). Then the array is filled with a constant value and intensity distribution histogram (i.e. the number of counts associated with a certain intensity value) can be obtained which is a discrete spectrum consisting of two peaks at absorption signals for the wafer (in ideal case at zero) and the gold structures (figure 35 *c*).

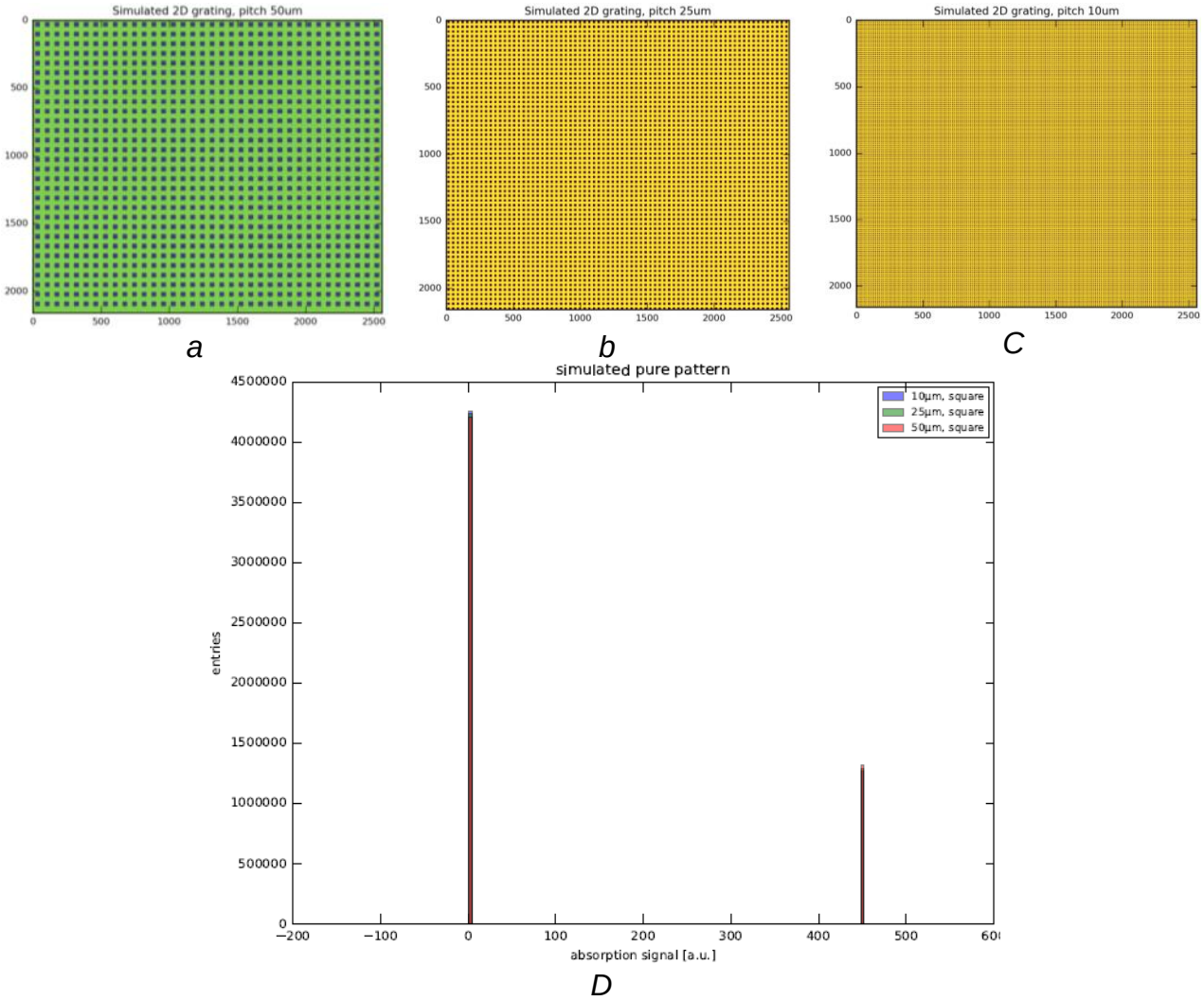

Figure 35 – Simulated data arrays – ideal gratings with periods *a*) 50 µm, *b*) 25 µm, *c*) 10µm and *d*) their intensity distribution histogram

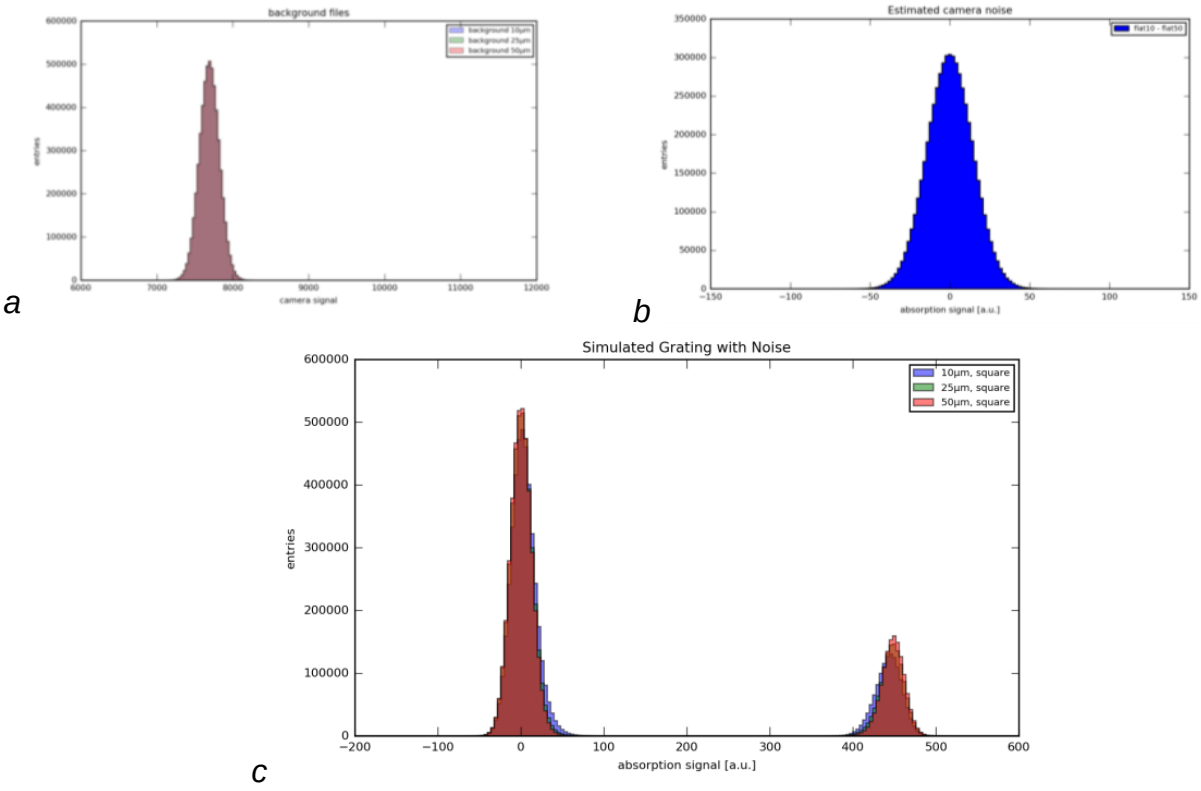

a b c

Figure 36 – Simulations for ideal gratings: a) flat-field image without the wafer with added blurring of the distribution due to the camera noise Gaussian detector noise, b) estimated camera noise with wafer absorption considered and c) intensity distribution histogram

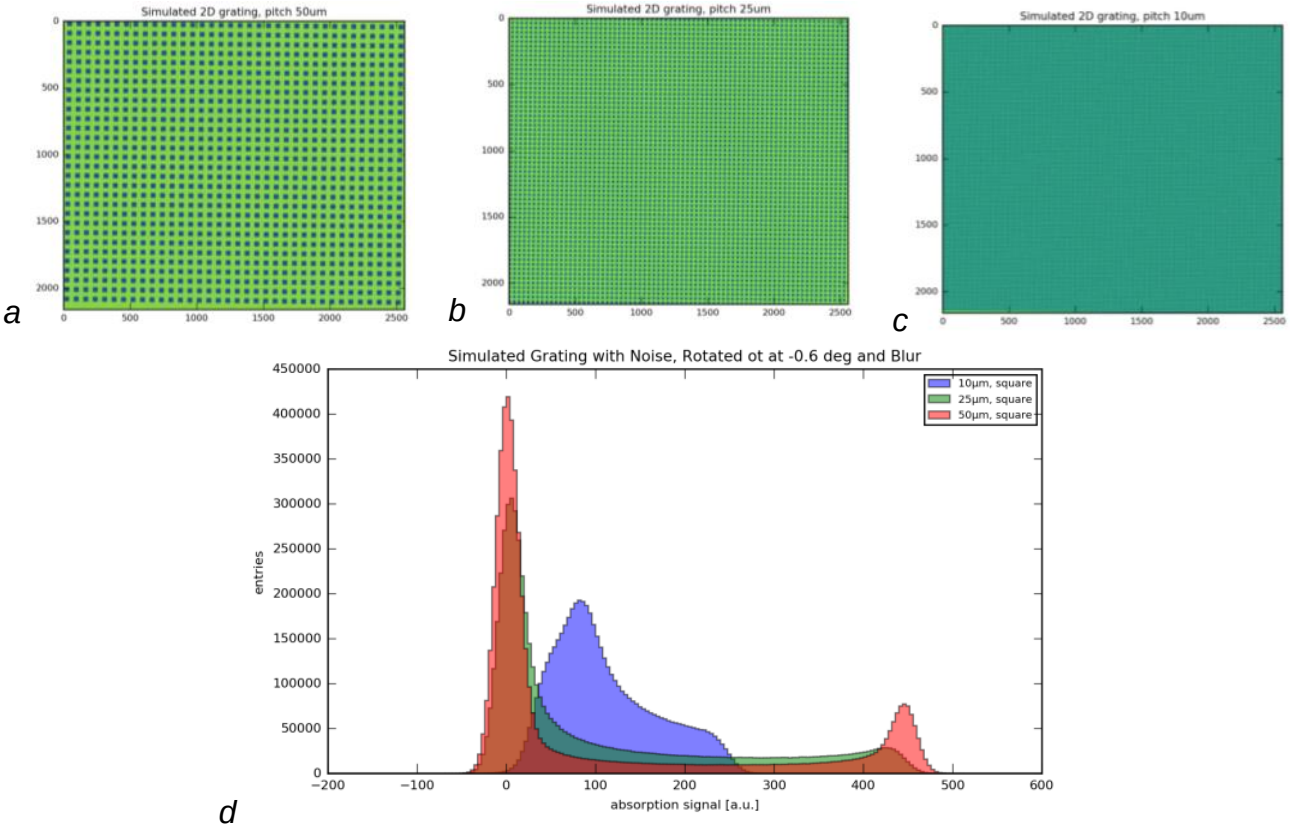

a b c d

Figure 37 – Simulated tilted data arrays – blurred by background and tilted at -0.6 ºwith respect to *y*-axis ideal gratings with periods *a*) 50 µm, *b*) 25 µm, *c*) 10 µm and *d*) their intensity distribution histogram with 3x3 median filter to remove pixel-noise

When the arrays and associated intensity distribution histograms are obtained, it is necessary to approximate real grating by adding background function. This can be done by introducing random fluctuations around central value as camera noise – Gaussian distribution (figure 36 *a*). As the grating is supported by the substrate, it introduces a certain absorption, which decreases signal to noise ratio. Thus, the camera noise was further estimated taking into account the absorption of the 200 μm thick silicon wafer (figure 36 *b*).

However in reality not only the presence of camera noise distorts the intensity distribution, but also the fact that the grating might be tilted with respect to y-axis (figure 37 *a-c*) which leads to significant blurring of distribution especially for smaller periods such as 10 μm (figure 37 *d*). One can see that for the simulated grating with 10 μm period intensity distribution is not discrete anymore and peaks associated with absorption of the wafer and the structures are merged and not clearly distinguished, which is due to the presence of entries of intermediate intensity value. This means that such a rotation angle is critical for 10 μm period and thus one should pay a special attention to the alignment while using the gratings of smaller periods. All the simulations were performed using high-level programming language Python with the support of scientific supervisor.

3.3.3 Testing of developed algorithm within radiography setup

Testing of the developed algorithm was performed using radiographic data obtained at TopoTomo beamline of ANKA synchrotron facility (Karlsruhe, Germany). We express our gratitude to beamline scientist Tomy dos Santos Rolo for supporting the measurement. Parameters of the setup arrangements are listed in table 6.

Table 6 – Setup parameters used for grating testing at TopoTomo beamline of ANKA synchrotron facility

Setup component	**Parameters**	**Comment**
Source	E=8.5 keV ΔE/E=0.01 λ=1.4586 Angstrom	TopoTomo beamline ANKA
Optical system	NA=0.28, Magnification = 10x, 180mm Tube lens, Effective Magnitude 9x, Effective pixel size 0.72 μm	Mitutoyo LWD bright field objective
Detector	Detector pixel size 720nm FoV = 2560 x 2140 pixels 6.5μm pixel pitch	Camera Andor Neo sCMOS
Arrangement	Distances: source-grating = 32 m, grating-detector ~8 cm	
Grating	Au pillars height = 15 μm, substrate (TiOx on Si) thickness = 200 μm	1460-2 wafer number

Radiographic images were obtained with only the gratings on the beam path. All four gratings which were manufactured on the wafer number 1460-2 were imaged. The

fragments of the images are shown in the figures 38 *a-c.* Flat-field images were obtained as well for each grating to correct histograms due to beam shape (figure 38 *e*) and estimate camera noise (figure 38 *f*). Utilizing all the data, histograms of intensity distributions for each square grating were plotted applying 3x3 median filters for pixel-noise removal to study the influence of the grating period on intensity distribution. From radiographic data (figure 38 *a-c*) and its analysis (figure 38 *e-g*) it follows that intensity distribution peaks for gratings of periods 50 μm and 25 μm are clearly separated, which means they can be successfully introduced in X-ray radiography setup to perform single-shot imaging as they provide with sufficient wavefront modulation. Although for the grating of period 10 μm WFM is not evident, this can be caused by several factors strongly appearing for smaller periods such as:

a) inhomogeneity of the gold structures height;

b) edge profile of fabricated structures: sloping sidewalls of the gold structures due to diffraction limit of photolithography;

c) misalignment due to rotation of the grating with respect to y-axis.

Possible solutions of this problem might be application of more sensitive to UV light photoresist or utilization of radiation with shorter wavelengths (deep UV or deep X-ray lithography).

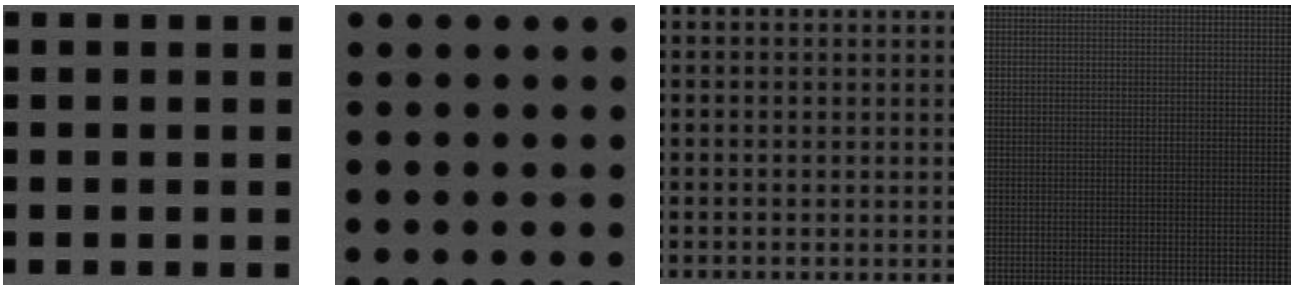

a *b* *c* *d*

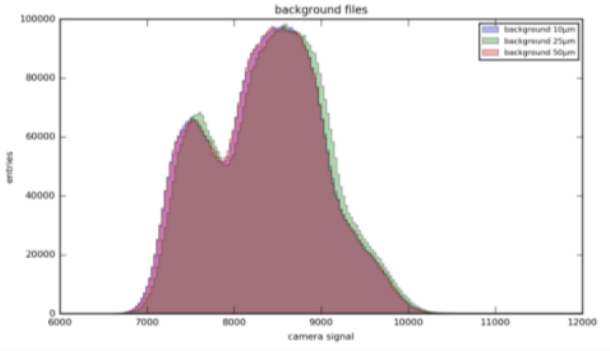

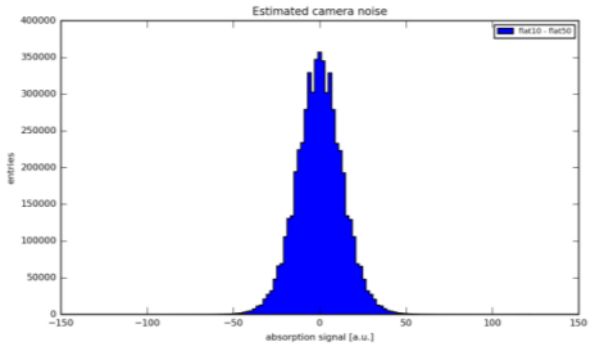

e *f*

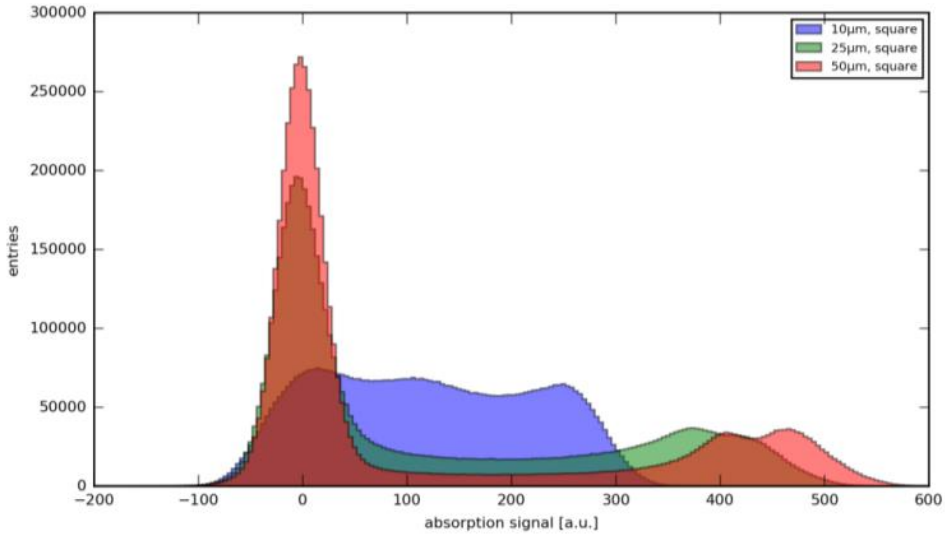

g

Figure 38 – Fragments of the radiographic images obtained for *a)* 50 µm period square structures, *b)* 50 µm period round structures, *c)* 25 µm period square structures and *d)* 10 µm square structures. Data obtain in experiment at TopoTomo beamline from flat-field image: *e)* background function, *f)* estimated camera noise and *g)* histograms of intensity distribution for each square grating with 3x3 median filter to remove pixel-noise

Conclusions and Outlook

In this work short overview of single-shot imaging techniques with emphasis on Fourier analysis based spatial harmonic imaging was made with a brief comparison of their advantages and disadvantages. Based on the comparative literature review requirements imposed on the grating structures were formulated.

Technological process was developed for two-dimensional grating manufacturing using photolithography and electroforming in order to meet the requirements imposed by the spatial harmonic imaging method. Two-dimensional gratings of high quality were manufactured with different periods and gold structure height ensuring efficient WFM for different energies up to 28 keV. Gratings quality was assessed with SEM and in the radiography setup using self-developed algorithm based on histograms of intensity distribution. It was shown that positioning of the grating becomes crucial for 10 μm grating periods, while the gratings of 25 and 50 μm periods are quite tolerant to small rotation of the grating with respect to the y-axis.

It is out intension to continue improving gratings quality towards higher aspect ratios in order to make available singe-shot imaging at higher energies with sufficient two-dimensional wavefront modulation provided by the gratings. Further work can be connected with photoresist optimization in order to tune its sensitivity and overall performance as well as with adaptation of the technological fabrication process for shorter wavelengths, e.g. deep X-ray lithography.

Future work will be focused on implementation of developed gratings in X-ray imaging setups to respond to various medical and materials science related applications. It is planned to improve the contrast due to utilization of high quality optical components and to investigate the capabilities of spatial harmonic single-shot imaging with inherent particle-size sensitivity of scattering signal.

Глава 4 Финансовый менеджмент, ресурсоэффективность и ресурсосбережение

4.1 Предпроектный анализ

4.1.1 Потенциальные потребители результатов исследования

Продукт: двумерные рентгеновские дифракционные решетки для ренгенорадиографических исследования различных слабопоглощающих объектов.

Целевой рынок: компании и научные центры, разрабатывающие методы мониторинга слабопоглощающих объектов с использованием рентгеновского излучения: Rigaku, Bruker, Siemens, Hammamatsu, Excillum Sigray, Paul Scherrer Institute (PSI), Technical University Munich (TUM).

4.1.2 Анализ конкурентных технических решений с позиции ресурсоэффективности и ресурсосбережения

Анализ рынка показал наличие двух основных конкурентов для производимого продукта – это производители расходных материалов для электронной и оптической микроскопии, двумерные решетки которых может быть использованы и для рентгеновской радиографии. Основные характеристики, определяющие ресурсоэффективность и экономическую эффективность, приведены в таблице 1. Оценочная карта для сравнения конкурентных технических разработок на основе этих критериев приведена в таблице 2.

Таблица 4.1 – Конкурентные технические разработки

Номер (*i*)	Произоводитель	Тип продукции	Стоимость
1	Автор проекта	дифракционная решётка: толщина до 30 мкм, период 50 мкм и 25 мкм, размер 10 мм.	400 евро
2	Structure Probe Inc. Consumables	решётка для калиброки микроскопа (сетка) 02799G-AB: толщина 2,5-5 мкм, период 34,6 мкм, размер 25,4 мм.	320 евро
3	Electron Microscopy Sciences	решётка для пропускающей электронной микроскопии (сетка) G400-Au: толщина 18 мкм, период 62 мкм, размер 3,05 мм.	50 евро

Таблица 4. 2 - Оценочная карта для сравнения конкурентных технических разработок

Критерии оценки	Вес крите-рия	Баллы			Конкуренто-способность		
		$Б_1$	$Б_2$	$Б_3$	$К_1$	$К_2$	$К_3$
1	2	3	4	5	6	7	8
Технические критерии оценки ресурсоэффективности							
1. Удобство в эксплуатации (соответствует требованиям потребителей)	0,11	5	3	4	0,55	0,33	0,44
2. Помехоустойчивость	0,02	5	3	5	0,1	0,06	0,1
3. Энергоэкономичность	0,1	5	4	3	0,5	0,4	0,3
4. Надежность	0,05	5	3	5	0,25	0,15	0,25
5. Уровень шума	0,02	5	3	4	0,1	0,06	0,08
6. Функциональная мощность (предоставляемые возможности)	0,15	5	3	3	0,75	0,45	0,45
7. Простота эксплуатации	0,1	5	5	3	0,5	0,5	0,3
Экономические критерии оценки эффективности							
1. Конкурентоспособность продукта	0,08	5	4	4	0,4	0,4	0,32
2. Уровень проникновения на рынок	0,05	4	5	5	0,2	0,25	0,25
3. Цена	0,09	3	4	5	0,27	0,36	0,45
4. Предполагаемый срок эксплуатации	0,09	5	3	4	0,45	0,27	0,36
5. Послепродажное обслуживание	0,03	4	5	5	0,12	0,15	0,15
6. Финансирование научной разработки	0,05	4	5	5	0,2	0,25	0,25
7. Срок выхода на рынок	0,05	5	5	5	0,25	0,25	0,25
8. Наличие сертификации разработки	0,05	4	5	5	0,2	0,25	0,25
Итого	**1**	**70**	**60**	**65**	**4,93**	**4,13**	**4,2**

Основываясь на знаниях о конкурентах, можно сделать вывод, что уязвимость позиции конкурентов связана с:

- малым размером решетки, что влечет за собой снижение удобства и простоты эксплуатации, а также значительно ограничивает функциональную мощность продукции. Таким образом, снижается конкурентоспособность решетки, предполагаемый срок эксплуатации (в случае частичного разрушения структур невозможно использовать другие участки решетки), однако уменьшение расхода золота позволяет снизить стоимость;
- малой толщиной решетки, что влечет за собой снижение удобства использования, помехоустойчивости, надежность, уровень шума, а также

значительно снижает количество возможностей применения, т.к. малая толщина влечет за собой слабую модуляцию волнового фронта излучения. Кроме того, срок экспуатации в данном случае снижается из-за увеличения вероятности повредить тонкую решетку вследствие радиационно-индуцированных дефектов.

Таким образом, конкурентным преимуществом дифракционных решеток является их универсальность. Производство высококачественных решеток достаточно большой площади и толщины позволяет занять свою нишу на рынке оптической продукции.

4.1.3 SWOT-анализ

SWOT – Strengths (сильные стороны), Weaknesses (слабые стороны), Opportunities (возможности) и Threats (угрозы) – представляет собой комплексный анализ научно-исследовательского проекта.

Таблица 4. 3 – SWOT-анализ

	Сильные стороны научно-исследовательского проекта: С1. Универсальность использования продукции. С2.Более высокое качество продукции по сравнению с конкурентами. С3. Востребованность продукции. С4.Доступная технология производства. С5.Наличие широкой инструментальной базы для создания и оптимизации продукции. С6.Квалифицированный персонал.	**Слабые стороны научно-исследовательского проекта:** Сл1. Более выоская стоимость конечного продукта. Сл2.Отсутствие возможности массового производства. Сл3.Отсутствие необходимого оборудования для проведения испытания опытного образца. Сл4. Большой срок поставок материалов и комплектующих, используемых при проведении научного исследования.
Возможности: В1.Использование инновационной инфраструктуры Института Микротехнологий (Карлсруэ, Германия) В2.Появление дополнительного спроса на новый продукт В3. Снижение расхода золота или замена его более дешевым материалом (например, свинец).	**СиВ:** Разработка различных видов дифракционных решеток с целью оптимизации их работы, получения продукта с конкурентными преимуществами с оптимальной себестоимостью, доступной технологией производства и высоким качеством.	**СЛиВ:** 1. Снижение стоимости продукции за счет снижения расхода золота или замены его аналогом, 2.Расширение инструкментальной базы для получения возможности массового произодства и испытания опытного образца, 3.сокращение поставок или смена поставщика.

В4. Повышение стоимости конкурентных разработок		
Угрозы: У1.Отсутствие спроса на новые технологии производства У2.Развитая конкуренция технологий производства У3.Введение дополнительных государственных требований к сертификации продукции	**СВиУ:** 1.Продвижение программы с целью создания спроса 2.Создание конкурентных преимуществ готового продукта 3.Сертификация и стандартизация продукта	**СЛиУ:** 1.Разивитие технологих рентгеновской визуализации у потенциальных потребителей 2.Приобретения необходимого оборудования для проведения испытания опытного образца 3.Сокращение поставок или смена поставщика 4. Продвижение программы с целью создания спроса путем демонстрации преимуществ при работе решетками 5.Создание конкурентных преимуществ готового продукта 6.Сертификация и стандартизация продукта

4.1.4 Оценка готовности проекта к коммерциализации

Таблица 4.4 – Бланк оценки степени готовности научного проекта к коммерциализации

№ п/п	Наименование	Степень проработанности научного проекта	Уровень имеющихся знаний у разработчика
1.	Определен имеющийся научно-технический задел	4	5
2.	Определены перспективные направления коммерциализации научно-технического задела	4	4
3.	Определены отрасли и технологии (товары) для предложения на рынке	5	5
4.	Определена товарная форма научно-технического задела для представления на рынок	5	4
5.	Определены авторы и осуществлена охрана их прав	4	5
6.	Проведена оценка стоимости интеллектуальной собственности	4	4
7.	Проведены маркетинговые исследования рынков сбыта	3	3
8.	Разработан бизнес-план коммерциализации научной разработки	2	2
9.	Определены пути продвижения	3	4

	научной разработки на рынок		
10.	Разработана стратегия (форма) реализации научной разработки	5	5
11.	Проработаны вопросы международного сотрудничества и выхода на зарубежный рынок	5	5
12.	Проработаны вопросы использования услуг инфраструктуры поддержки, получения льгот	2	2
13.	Проработаны вопросы финансирования коммерциализации научной разработки	2	3
14.	Имеется команда для коммерциализации научной разработки	2	2
15.	Проработан механизм реализации научного проекта	2	3
	ИТОГО БАЛЛОВ:	52	56

По результатам оценки готовности проекта к коммерциализации и уровеня имеющихся знаний у разработчика (таблица 4.4) было установлено, что проект обладает перспективностью выше среднего, что говорит о целесооборазности инвестирования в текущую разработку и направления ее дальнейшего улучшения. Разработчик обладает достаточным уровнем компетенций, однако возомжно привлечение в команду проекта специалистов, ответственных за коммерческую реализацию продукции.

4.2 Инициация проекта

Группа процессов инициации состоит из процессов, которые выполняются для определения нового проекта или новой фазы существующего. В рамках процессов инициации определяются изначальные цели и содержание и фиксируются изначальные финансовые ресурсы. Определяются внутренние и внешние заинтересованные стороны проекта, которые будут взаимодействовать и влиять на общий результат научного проекта. Данная информация закрепляется в Уставе проекта.

Таблица 4.5 – *Заинтересованные стороны проекта*

Заинтересованные стороны проекта	**Ожидания заинтересованных сторон**
Институт Микротехнологий Техологического института Карлсруэ, Национальный исследовательский Томский политехнический универитет	Создание новых оптических элементов и их оптимизация/усовершенствование

Таблица 4.6 – Цели и результат проекта

Цели проекта:	Разработка двумерных решеточных структур методами оптической литографии и электроосаждения оценка их качетва для использования в ренгенорадиографических исследованиях различных слабопоглощающих объектов.
Ожидаемые результаты проекта:	Получение двумерных дифракционных решеток высокого качества с различными характеристикам, а также оптимизированного технологического процесса их создания и оценки качества.
Критерии приемки результата проекта:	Адекватность результатов
Требования к результату проекта:	**Требование:**
	Стандартизация готового продукта

Организационная структура проекта

Таблица 4.7 – Рабочая группа проекта

№ п/п	**ФИО, основное место работы, должность**	**Роль в проекте**	**Функции**	**Трудо-затраты, час.**
1	Крючков Юрий Юрьевич, НИ ТПУ, кафедра общей физики, профессор, д.ф.-м.н.	Руководитель	Координация деятельности проекта	60
2	Захарова Маргарита Анатольевна, НИ ТПУ, кафедра общей физики, магистрант	Исполнитель	Выполнение НИР	500
			ИТОГО:	560

Таблица 4.8 – Ограничения проекта

Фактор	Ограничения/ допущения
3.1. Бюджет проекта	193 216,2
3.1.1. Источник финансирования	Институт Микротехнологий Техологического института Карлсруэ, НИ ТПУ
3.2. Сроки проекта:	20.02.17-20.05.17
3.2.1. Дата утверждения плана управления проектом	10.01.17
3.2.2. Дата завершения проекта	20.05.17

4.3 Планирование управления научно-техническим проектом

4.3.1. План проекта

Линейный график представляется в виде таблицы (табл. 8).

Таблица 4. 9 – Календарный план проекта

Название	**Длительность, раб дни**	**Дата начала работ**	**Дата окончания работ**	**Состав участников**
Обсуждение целей и задач, планирование	5	20.02	24.02	Захарова Маргарита Анатольевна, Крючков Юрий Юрьевич
Изучение литературы, составление литературного обзора	16	25.02	12.03	Захарова Маргарита Анатольевна
Оптимизация процесса литографии двумерных структур заданной высоты	21	13.03	02.04	Захарова Маргарита Анатольевна
Создание двумерных решеток и оценка их качества	28	03.04	30.04	Захарова Маргарита Анатольевна
Обсуждение полученных результатов	7	01.05	07.05	Захарова Маргарита Анатольевна, Крючков Юрий Юрьевич
Оформление выводов	3	08.05	10.05	Захарова Маргарита Анатольевна
Оформление пояснительной записки	10	11.05	20.05	Захарова Маргарита Анатольевна
Итого:	90	20.02	20.05	

Таблица 4.10 – Календарный план-график проведения НИОКР по теме

Вид работ	Исполнители	$T_к$, дн.	Продолжительность выполнения работ										
			февр			март			апрель			май	
			1	2	3	1	2	3	1	2	3	1	2
Обсуждение целей и задач, планирование	Маг-нт Рук-ль	18											
Изучение литературы, составление литературного обзора	Маг-нт	21											
Оптимизация процесса литографии двумерных структур заданной высоты	Маг-нт	15											
Создание двумерных решеток и оценка их качества	Маг-нт	15											
Обсуждение полученных результатов	Маг-нт Рук-ль	7											
Оформление выводов	Маг-нт	3											
Оформление пояснительной записки	Маг-нт	10											

магистрант руководитель

4.3.2. Бюджет научного исследования

Сырье, материалы, покупные изделия и полуфабрикаты (за вычетом отходов)

Таблица 4.11 – Группировка затрат по статьям

Затраты по статьям					
Сырье, материалы (за вычетом возвратных отходов), покупные изделия и полуфабрикаты	Специальное оборудование для научных (экспериментальных) работ	Основная заработная плата	Дополнительная заработная плата	Отчисления на социальные нужды	Итого плановая себестоимость
35 120,8	40 920,0	80 477,6	9 657,3	27 040,5	193 216,2

Таблица 4.12 – Сырье, материалы, комплектующие изделия и покупные полуфабрикаты

Наименование	Марка, размер	Кол-во	Цена за единицу, руб.	Сумма, руб.
Фоторезист	mr-x 10, MicroChem, 1 литр (бутылка)	200 мл	49 600	9 920
Проявитель	Пропиленгликоль монометил эфир ацетат	1 л	3 000	3 000
Изопропиловый спирт		1 л	250	250
Подложка из кремния	толщина 200 мкм	6	3 100	18 600
Золото		2 г	1000	2000
Всего за материалы				33 770,0
Транспортно-заготовительные расходы (3-5%)				1 350,8
Итого по статье $C_м$				35 120,8

В эту статью включаются затраты на приобретение расходных материалов, необходимых для изготовления дифракционных решеток методом фотолитографии и электроосаждения. Всего было изготовлено 5 готовых к использованию решеток.

Специальное оборудование для научных (экспериментальных) работ

Таблица 4.13 – Расчет затрат по статье «Спецоборудование для научных работ»

№ п/п	Наименование оборудования	Кол-во единиц оборудования	Цена единицы оборудования, тыс.руб.	Общая стоимость оборудования, тыс.руб.
1.	Фотомаска (Хром-кварц)	1	40,92	40,92

В данную статью включены затраты, связанные с приобретением фотомаски для облучения подготовленных образцов. Фотомаска была приобретена у фирмы

Compugraphics (Йена, Германия) за счет средств Институт Микротехнологий Техологического института Карлсруэ.

Основная заработная плата

Таблица 4.14 - Баланс рабочего времени

Показатели рабочего времени	Руководитель	Магистр
Календарное число дней	90	90
Количество нерабочих дней - выходные дни - праздничные дни	22 12	27 4
Потери рабочего времени - отпуск - невыходы по болезни	-	-
Действительный годовой фонд рабочего времени	56	59

Вследствие того, что экспериментальные работы по проекту проходили в Германии и были проведены магистрантом, а руководство совершалось из ТПУ, количество праздничных дней различно. При этом студент на время выполнения проекта получал стипендию Дома молодых ученых Карлсруэ от Германской службы академических обменов.

Таблица 4.15 – Расчёт основной заработной платы

Исполнители	$З_б$, руб.	$k_р$	$З_м$, руб	$З_{дн}$, руб.	$Т_р$, раб.дн.	$З_{осн}$, руб.
Руководитель	33 162,9	1,3	43 111,7	1 437,1	56	80 477,6
Магистрант	-	-	-	-	59	-

Дополнительная заработная плата научно-производственного персонала

Таблица 4.16 – Заработная плата исполнителей НТИ

Заработная плата	Руководитель	Магистрант
Основная зарплата	80 477,6	-
Дополнительная зарплата	9 657,3	-
Итого по статье $C_{зп}$	90 134,9	-

Отчисления на социальные нужды

Статья включает в себя отчисления во внебюджетные фонды.

$$C_{внеб} = k_{внеб} \cdot (З_{осн} + З_{доп}), \quad (8)$$

где $k_{внеб}$ =30 % коэффициент отчислений на уплату во внебюджетные фонды (пенсионный фонд, фонд обязательного медицинского страхования и пр.).

Таблица 4.17 – Отчисления на социальные нужды

	Руководитель	Магистрант

Зарплата	90 134,9	-
Отчисления на социальные нужды	27 040,5	-

4.3.3. Организационная структура проекта

Таблица 4.18 – Выбор организационной структуры научного проекта

Критерии выбора	Функциональная	Матричная	Проектная
Степень неопределенности условий реализации проекта	Низкая	Высокая	Высокая
Технология проекта	Стандартная	Сложная	Новая
Сложность проекта	Низкая	Средняя	Высокая
Взаимозависимость между отдельными частями проекта	Низкая	Средняя	Высокая
Критичность фактора времени (обязательства по срокам завершения работ)	Низкая	Средняя	Высокая
Взаимосвязь и взаимозависимость проекта от организаций более высокого уровня	Высокая	Средняя	Низкая

На основе проведенного анализа выбора организационной структуры научного проекта, было выявлено, что наиболее выгодной является матричная структура.

4.4 Определение ресурсной (ресурсосберегающей), финансовой, бюджетной, социальной и экономической эффективности исследования

Эффективность научного ресурсосберегающего проекта включает в себя социальную эффективность, экономическую и бюджетную эффективность. Показатели общественной эффективности учитывают социально-экономические последствия осуществления инвестиционного проекта как для общества в целом, в том числе непосредственные результаты и затраты проекта, так и затраты, и результаты в смежных секторах экономики, экологические, социальные и иные внеэкономические эффекты.

Показатели экономической эффективности проекта учитывают финансовые последствия его осуществления для предприятия, реализующего данный проект. В этом случае показатели эффективности проекта в целом характеризуют с экономической точки зрения технические, технологические и организационные проектные решения.

Бюджетная эффективность характеризуется участием государства в проекте с точки зрения расходов и доходов бюджетов всех уровней.

4.4.1. Динамические методы экономической оценки инвестиций

Динамические методы оценки инвестиций базируются на применении показателей:

- чистая текущая стоимость ($\mathbf{NPV}$);
- срок окупаемости ($\mathbf{PP}$);
- внутренняя ставка доходности ($\mathbf{IRR}$);
- индекс доходности ($\mathbf{PI}$).

Все перечисленные показатели основываются на сопоставлении чистых денежных поступлений от операционной и инвестиционной деятельности, и их приведении к определенному моменту времени. Теоретически чистые денежные поступления можно приводить к любому моменту времени (к будущему либо текущему периоду). Но для практических целей оценку инвестиции удобнее осуществлять на момент принятия решений об инвестировании средств.

4.4.2. Чистая текущая стоимость ($\mathbf{NPV}$)

Данный метод основан на сопоставлении дисконтированных чистых денежных поступлений от операционной и инвестиционной деятельности.

Если инвестиции носят разовый характер, то $\mathbf{NPV}$ определяется по формуле

$$\mathbf{NPV} = \sum_{t=1}^{n} \frac{\mathbf{ЧДП_{оп_t}}}{(1+i)^t} - \mathbf{I_0}, \qquad (9)$$

где $\mathbf{ЧДП_{оп_t}}$ – чистые денежные поступления от операционной деятельности;

$\mathbf{I_0}$ – разовые инвестиции, осуществляемые в нулевом году;

$\mathbf{t}$ – номер шага расчета ($\mathbf{t}$ = 0, 1, 2… $\mathbf{n}$);

$\mathbf{n}$ – горизонт расчета;

$\mathbf{i}$ – ставка дисконтирования (желаемый уровень доходности инвестируемых средств).

Чистая текущая стоимость является абсолютным показателем. Условием экономичности инвестиционного проекта по данному показателю является выполнение следующего неравенства: $\mathbf{NPV} > 0$.

Чем больше **NPV**, тем больше влияние инвестиционного проекта на экономический потенциал предприятия, реализующего данный проект, и на экономическую ценность этого предприятия.

Таким образом, инвестиционный проект считается выгодным, если **NPV** является положительной.

Таблица 4.19 - Расчет чистой текущей стоимости по проекту в целом

№	Наименование показателей	Шаг расчета				
		0	1	2	3	4
1.	Выручка от реализации, тыс.руб	0	241,520	241,520	241,520	241,520
2.	Итого приток	0	241,520	241,520	241,520	241,520
3.	Инвестиционные издержки, тыс.руб.	-193,216	0	0	0	0
4.	Операционные затраты, тыс. руб С+Ам+ФОТ	0	48,304	48,304	48,304	48,304
4.1	Налогооб прибыль=п.1-п.4	0	193,216	193,216	193,216	193,216
5.	Налоги Выр-опер=донал.приб*20%	0	38,643	38,643	38,643	38,643
6.	Итого отток Опер.затр+налоги	-193,216	86,947	86,947	86,947	86,947
6.1	Чистая прибыль (4.1-5) Или (1-6)	0	154,573	154,573	154,573	154,573
7.	Чистый денежный поток ЧДП=Пчист+Ам Пчист=Пдонал.-налог	-193,216	154,573	154,573	154,573	154,573
8.	Коэффициент дисконтирования (приведения при **i** = 0,20)	1,0	0,83	0,69	0,58	0,48
9.	Дисконтированный чистый денежный поток (с7*с8)	-193,216	128,296	106,655	89,652	74,195
10.	То же нарастающим итогом (**NPV** = 206,932)	-193,216	-64,405	42,937	132,389	206,932

Таким образом, чистая текущая стоимость по проекту в целом составляет 206 932 д. ед., что позволяет судить о его эффективности.

4.4.3 Дисконтированный срок окупаемости

Как отмечалось ранее, одним из недостатков показателя простого срока окупаемости является игнорирование в процессе его расчета разной ценности денег во времени.

Этот недостаток устраняется путем определения дисконтированного срока окупаемости.

Рассчитывается данный показатель примерно по той же методике, что и простой срок окупаемости, с той лишь разницей, что последний не учитывает фактор времени.

Наиболее приемлемым методом установления дисконтированного срока окупаемости является расчет кумулятивного (нарастающим итогом) денежного потока (см. табл. 4.20).

Таблица 4.20 - Дисконтированный срок окупаемости

№	Наименование показателя	Шаг расчета				
		0	1	2	3	4
1.	Дисконтированный чистый денежный поток	-193,216	128,296	106,655	89,652	74,195
2.	То же нарастающим итогом	-193,216	-64,405	42,937	132,389	206,932
3.	Дисконтированный срок окупаемости	$PP_{дск}$ =1+64,405/106,655 = 0,60года ≈ 7 месяцев				

4.4.4 Внутренняя ставка доходности (IRR)

Для установления показателя чистой текущей стоимости (NPV) необходимо располагать информацией о ставке дисконтирования, определение которой является проблемой, поскольку зависит от оценки экспертов. Поэтому, чтобы уменьшить субъективизм в оценке эффективности инвестиций на практике широкое распространение получил метод, основанный на расчете внутренней ставки доходности (IRR).

Между чистой текущей стоимостью (NPV) и ставкой дисконтирования (i) существует обратная зависимость. Эта зависимость следует из таблицы 4.21 и графика, представленного на рисунке 39.

Таблица 4.21 - Зависимость NPV от ставки дисконтирования

№ п/п	Наименование показателя	0	1	2	3	4	NPV
1	Чистые денежные потоки	-193 216	154 573	154 573	154 573	154 573	
2	коэффициент дисконтирования						
	i=0,1	1	0,909	0,826	0,751	0,683	
	i=0,2	1	0,833	0,694	0,578	0,482	
	i=0,4	1	0,714	0,51	0,364	0,26	
	i=0,5	1	0,667	0,444	0,295	0,198	

	i=0,6	1	0,625	0,390	0,244	0,095	
	i=0,7	1	0,588	0,335	0,203	0,070	
3	Дисконтированный денежный поток						
	i=0,1	-193 216	140 507	127 677	116 084	105 573	296 625
	i=0,2	-193 216	128 759	107 274	89 343	74 504	206 664
	i=0,4	-193 216	110 365	78 832	56 265	40 189	92 435
	i=0,5	-193 216	103 100	68 630	45 599	30 605	54 718
	i=0,6	-193 216	96 608	60 283	37 716	14 684	16 075
	i=0,7	-193 216	90 889	51 782	31 378	10 820	-8 337

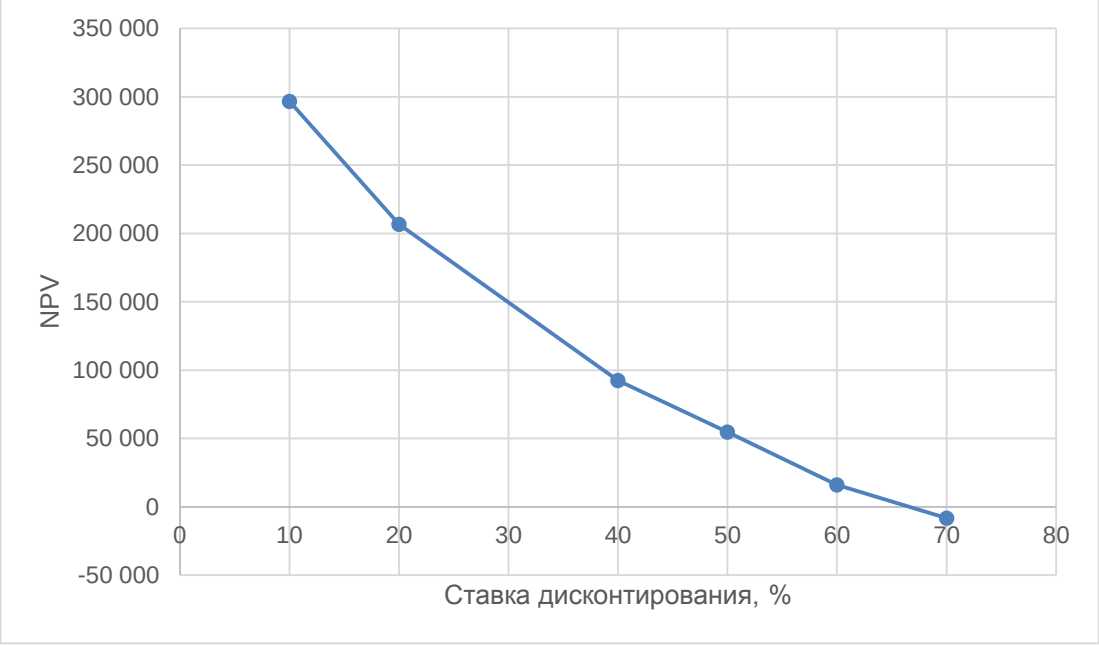

Рисунок 39 – Зависимость NPV от ставки дисконтирования

Из таблицы и графика следует, что по мере роста ставки дисконтирования чистая текущая стоимость уменьшается, становясь отрицательной. Значение ставки, при которой **NPV** обращается в нуль, носит название «внутренней ставки доходности» или «внутренней нормы прибыли». Из графика получаем, что **IRR** составляет 0,67 > 0,2.

4.4.5 Индекс доходности (рентабельности) инвестиций ($\mathbf{PI}$)

Индекс доходности показывает, сколько приходится дисконтированных денежных поступлений на рубль инвестиций. Расчет этого показателя осуществляется по формуле

$$PI = \sum_{t=1}^{n} \frac{ЧПД_t}{(1+i)^t} / I_0, \quad (10)$$

где I_0 – первоначальные инвестиции.

$$\text{PI} = \frac{128\,296 + 106\,655 + 89\,652 + 74\,195}{193\,216} = 2{,}06$$

PI = 2.06>1, следовательно, проект эффективен при i = 0,2.

4.5 Оценка сравнительной эффективности исследования

Интегральный показатель ресурсной эффективности вариантов исполнения объекта исследования можно определить следующим образом:

$$\text{I}_{\text{pi}} = \sum a_i \cdot b_i, \quad (11)$$

где I_{pi} – интегральный показатель ресурсоэффективности для i-го варианта исполнения разработки;

a_i – весовой коэффициент *i*-го варианта исполнения разработки;

b_i – бальная оценка *i*-го варианта исполнения разработки, устанавливается экспертным путем по выбранной шкале оценивания;

n – число параметров сравнения.

В качестве возможных вариантов исполнения выберем реализованный способ, а также два альтернативных варианта: вариант заказом на выполнение исследовательских работ у сторонней организации на оборудовании данной организации, а также вариант заказом на выполнение работ специалистами из сторонней организации, но на оборудовании, принадлежащем организации где выполняется исследование. Основным лимитирующим фактором в представленном НТИ являлась его стоимость. Заказ на выполнение работ у сторонней организации сократил бы рабочее время исполнителей темы, однако, привнес бы дополнительную статью расхода в размере 150000 руб. Третий представленный вариант является также невыгодным в отношении стоимости проекта. В затраты в этом случае войдут основная и дополнительная заработные платы для высококвалифицированных инженеров, соответствующие отчисления во

внебюджетные фонды, а также затраты на оформление для них производственных командировок. Согласно грубой оценке стоимость вышеуказанных затрат могла бы составлять порядка 250 000 руб.

Сравнительная оценка характеристик вариантов исполнения проекта представлена в таблице 4.22.

Проведем расчет интегрального показателя ресурсоэффективности для каждого варианта исполнения:

$$I_m^p = 5 \times 0,3 + 4 \times 0,1 + 5 \times 0,15 + 5 \times 0,15 + 4 \times 0,1 + 5 \times 0,2 = 4,8$$

$$I_1^A = 2 \times 0,3 + 3 \times 0,1 + 5 \times 0,15 + 3 \times 0,15 + 3 \times 0,1 + 4 \times 0,2 = 3,2$$

$$I_2^A = 3 \times 0,3 + 3 \times 0,1 + 4 \times 0,15 + 2 \times 0,15 + 3 \times 0,1 + 4 \times 0,2 = 3,2$$

Как видно из рассчитанных значений, вариант исполнения, который был реализован в данной работе, является наиболее ресурсоэффективным.

Таблица 4.22 – Сравнительная оценка характеристик вариантов исполнения проекта

Критерии	Весовой коэффициент параметра	Текущий проект	Аналог 1	Аналог 2
1. Удобство в эксплуатации (соответствует требованиям потребителей)	0,3	5	2	3
2. Помехоустойчивость	0,1	4	3	3
3. Энергоэкономичность	0,15	5	5	4
4. Надежность	0,15	5	3	2
5. Уровень шума	0,1	4	3	3
6. Функциональная мощность (предоставляемые возможности)	0,2	5	4	4
Итого	1	28	20	19

4.6 Выводы по главе

Из проделанных расчетов следует, что наибольшие затраты на научно-техническое исследование (более 45% от общей суммы) приходятся на оплату труда исполнителей темы (90 134,9 рублей) и порядка 40% затрат приходится на сырье и специальное оборудование. Это связано с тем, что в данной работе производится наукоемкая продукция, готовая к использованию и продаже, следовательно важно не

только проведение научных разработок, но и сырьевые затраты. В сумме же весь бюджет научно-технического исследования составляет 193 216,2 рубля.

В ходе проведения анализа показателей эффективности инвестиций была получена чистая текущая стоимость (NPV) – 206,932 руб. Таким образом, данный инвестиционный проект можно считать выгодным, NPV является положительной величиной. Дисконтированный срок окупаемости проекта составляет 7 месяцев. Внутренняя ставка доходности (IRR) – 0,67, что позволяет признать инвестиционный проект экономически оправданным, так как выполняется условие неравенства IRR>i. Индекс доходности (PI) – 2,06 и, основываясьна том, чтоданная величина превышает единицу, можно утверждать, что данная инвестиция приемлема.

Из расчета ресурсоэффективности также следует, что реализованный вариант исследования является наименее затратным. Данная оценка коммерческой ценности необходима, для представления состояния и перспективы проводимого научного исследования.

Literature

[1] S.W. Wilkins, Ya.I. Nesterets, T.E. Gureyev, S.C. Mayo, A. Pogany & A.W. Stevenson. On the evolution and relative merits of hard X-ray phase-contrast imaging methods // Phil. Trans. R. Soc., 2014. – A 372: 29130021. – 19p.

[2] F. Pfeiffer, M. Bench, O. Bunk, P. Kraft, E. F. Eikenberry, Ch. Brönnimann, C. Grünzweig & C. David. Hard-X-ray dark-field imaging using a grating interferometer // Nature Materials, 2008. – Vol. 7. – P. 134-137.

[3] T. Weitkamp, A. Diaz, David C. X-ray phase imaging with a grating interferometer // Optics Express, 2005. – Vol. 12. – No. 16. – P. 6296-6304.

[4] Kottler C., David C. Pfeiffer F., Bunk O. A two-dimensional approach for grating based differential phase contrast imaging using hard X-rays // Optics letters 2007, Vol.15, No.3. – P. 1175-1181.

[5] K. S. Morgan, D.M. Paganin & K.W. Siu. Quantitative single-exposure x-ray phase contrast imaging using a single attenuation grid // Optics express, 2011. – Vol.19. – No. 20. – P.19781-19789.

[6] H. Wen, E. Bennett, R. Kopace, A. Stein, V. Pai. Single-shot x-ray differential phase-contrast and diffraction imaging using two-dimensional transmission gratings // Optics Letters, 2010. – Vol. 35. – No.12. – P. 1932-1934.

[7] B. Wu, Ya. Liu, C. Rose-Petruck & G.J. Diebold. X-ray spatial frequency heterodyne imaging // Applied Physics Letters, 2012. – Vol. 100. – No. 061110 – 4 p.

[8] P. Bruza, D. Panek, M. Vrbova, V. Fidler & C. Rose-Petruck. Spatial frequency heterodyne imaging in soft x-ray water window // Applied Physics Letters, 2014. – Vol. 104. – No. 234101. – 4 p.

[9] D. Rand, Z. Derbak, R. Carlson, J.R. Wands & C. Rose-Petruck. X-ray Scatter Imaging of Hepatocellular Carcinoma in a Mouse Model Using nanoparticle Contrast Agents // Scientific Reports, 2015. – No.15673. – 1-14 p.

[10] D. Rand, E.G. Walsh, Z. Derdak, J.R. Wands & C. Rose-Petruck. A highly sensitive x-ray imaging modality for hepatocellular carcinoma detection *in vitro* // Phys. Med. Biol., 2015. – Vol.60. – P. 769-784.

[11] F.M. Schunk, D. Rand & C. Rose-Petruck. Spatial frequency heterodyne imaging of aqueous phase transitions inside multi-walled carbon nanotubes. Phys. Chem. Chem. Phys., 2015. – Vol.17. – P. 31237-31246.

[12] Ya. Liu, B. Ahr, A. Linkin, G.J. Diebold & C. Rose-Petruck. X-ray spatial harmonic imaging of phase objects // Optical Society of America, 2011. – Vol.36. – No.12. – P. 2209-2211.

[13] Kunka D., Mohr J., Nazimov V., Meiser J., Meyer P., Amberger M., Koch F., Schulz J., Walter M., Duttenhofer T., Voigt A., Ahrens G., Grützner G. Characterization method for new resist formulations for HAR patterns made by X-ray lithography // Microsystems Technology, 2014. – Vol. 20. No. 10. – P.2023-2029.

[14] F Krejci, J Jakubek & M Kroupa. Single grating method for low dose 1-D and 2-D phase contrast X-ray imaging // JINST, 2011. – Vol. 6. – No. C01073. – 10 p.

[15] McCord MA, Rooks MJ Resist in SPIE handbook of microlithography, micromatching and microfabrication. In: Rai-Choudhury (ed) Microlithography. – Vol. 1. – Section 2.7. – 2004.

[16] F. Pfeiffer, T. Weitkamp, O. Bunk, C. David. Phase retrieval and differential phase-contrast imaging with low-brilliance X-ray sources // Nature Physics, 2006. – Vol. 2. – P. 258-261.

[17] J. Mohr J., Grund T., Kunka D., Kenntner J., Leuthold J. High aspect ratio gatings f X-ray phase contrast imaging // AIP Conference Proceedings, 2012. – Vol. 1466. – P. 41-50.

[18] K. Scherer, L. Birnbacher, M. Chabior, J. Herzen, D. Mayr, S. Grandl, A. Sztrókay-Gaul, K. Hellerhoff, F. Bamberg, F. Pfeiffer. Bi-Directional X-Ray Phase-Contrast Mammography // PLoS ONE, 2014. – Vol. 9. – No. 5, e93502. – 7 p.

[19] I. Zanette, C. David, S. Rutishauser, T. Weitkamp. 2D grating simulation for X-ray phase-contrast and dark-field imaging with a Talbot interferometer // AIP Conference Proceedings, 2010. – Vol. 1221. – P. 73-79.

[20] H. Wen, E. E. Bennett, M. M. Hegedus, S. C. Carroll. Spatial Harmonic Imaging of X-ray Scattering – Initial results // IEEE Transactions on medical imaging, 2008. - Vol.27. – No. 8. – P.997-1002.

[21] F.Pfeiffer. Milestones and basic principles of grating-based x-ray and neutron phase-contrast imaging // AIP Conference Proceedings, 2012. – Vol. 1466. – P. 2-11.

[22] M. Shinohara, T.Yamashita, H.Tawa, M. Takeda, N. Sasaki, T. Takaya, R. Toh, A.Takeuchi, T. Ohigashi, K. Shinohara, S. Kawashima, M. Yokoyama, K. Hirata, A. Momose. Atherosclerotic plaque imaging using phase-contrast X-ray computed tomography // American Journal of Physiology - Heart and Circulatory Physiology, 2008. – Vol. 294. – No. 2. – P. 1094-1100.

[23] A. Malecki, E. Egg, F. Schaff, G. Potdevin, T. Baum, E.G. Garcia, J. S. Bauer, F. Pfeiffer. Correlation of X-Ray Dark-Field Radiography to Mechanical Sample Properties // Microsc. Microanal, 2014. – Vol. 20. – P. 1528–1533.

[24] V. Revol, I. Jerjen, C. Kottler, P. Schütz, R. Kaufmann, T. Lüthi, U. Sennhauser, U. Straumann, and C. Urban. Sub-pixel porosity revealed by x-ray scatter dark field imaging // Journal of Applied Physics, 2011. – Vol. 110. – No 4. - P. 044912.

[25] M.A. Beltran, D.M. Paganin, K.K.W. Siu, A.Fouras, S.B.Hooper, D.H. Reser, M.J. Kitchen. Interface-specific x-ray phase retrieval tomography of complex biological organs // Phys. Med. Biol., 2011. – Vol. 56. – P. 7353–7369.

[26] F. Krejci, J. Jakubek, M. Kroupa. Hard X-ray phase contrast imaging using single absorption grationg and hybrid semiconductor detector // Review of Scientific Instruments, 2010. – Vol. 81. – No.113702. – 5 p.

[27] M. Takeda, H. Ina, S. Kobayashi. Fourier-transform method of fringe-pattern analysis for computer-based topography and interferometry // J. Opt. Soc. Am., 1982. – Vol. 71. – No. 1. – P. 156-160.

[28] K. S. Morgan, D. M. Paganin, K.W. Siu. X-ray phase imaging with a paper analyzer // Appl. Phys. Lett., 2012. – Vol. 100. – No. 124102. – 4 p.

[29] P. Bruza. Pulsed Plasma soft X-ray source in biomedical research // Ph.D. Thesis. – Prague, 2014. – P. 21-61.

[30] E.E. Bennett, R. Kopace, A. F. Stein, H. Wen. A grating-based single-shot x-ray phase contrast and diffraction method for *in vivo* imaging // Med. Phys., 2010. – Vol. 37. – No.11. – P.6047-6054.

[31] S.K. Lynch, V. Pai, J. Auxier, A.F. Stein, E.E. Bennett, C.K. Kemble, X. Xiao, W.-K. Lee, N.Y. Morgan, H.H. Wen. Interpretation of dark-field contrast and particle-size selectivity in grating interferometers // Applied Optics, 2011. – Vol. 50. – No. 22. P. 4310-4319.

[32] A.F. Stein, J.Ilavsky, R.Kopace, E.E. Bennett, H. Wen. Selective imaging of nano-particle contrast agents by single-shot x-ray diffraction technique // Optics letters, 2010. – Vol.18. – No.12. – P. 13271-13278.

[33] G. Weber (n.d.). X-Ray attenuation & absorption calculator. Retrieved from website: http://web-docs.gsi.de/~stoe_exp/web_programs/x_ray_absorption/index.php

[34] D.R. Hines, N.P. Siwak, L.A. Mosher, R. Ghodssi. MEMS Lithography and Micromachining Techniques // MEMS Materials and Processes Handbook. – Springer US, 2011. – P. 667-753.

[35] T. Akinwande, R. O'Handley. Lectures 6.152J/3.155J on Microelectronics Processing Technology. Massachusetts Institute of Technology. Retrieved from the Microsystem Technology laboratories (MIT) website: URL http://www-mtl.mit.edu/researchgroups/hackman/6152J/LectureHandouts.html

[36] M.S. Hibbs: System Overview of Optical Steers and Scanners, Chapter 1, In J.R. Sheats, B.W. Smith (Eds.): Microlithography Science and Technology (Marcel Dekker, New York, NY, 1998).

[37] C.A. Mack. The Lithography Tutor Photoresist Development // FINLE Technologies. – Texas, 1994. Retrieved from the website. URL: http://www.lithoguru.com/scientist/litho_tutor/TUTOR08%20(Autumn%2094).pdf

[38] Processing Guidelines – Negative Photoresist Series mr-X // Micro resist technology, 2016. – 4 p.

[38] MicroChemicals GmbH. TI PRIME technical data sheet, revised 08/2016. Retrieved from the MicroChemicals website. URL: http://microchemicals.com/micro/tds_ti_prime.pdf